Systematic Transmission Electron Microscopy-Based Identification and 3D Reconstruction of Cellular Degradation Machinery

Kit Neikirk[1,2†], Zer Vue[2†], Prasanna Katti[3†], Ben I. Rodriguez[2], Salem A. Omer[2], Jianqiang Shao[4], Trace Christensen[5], Edgar Garza Lopez[2], Andrea Marshall[2], Caroline B. Palavicino-Maggio[6], Jessica Ponce[7], Ahmad Alghanem[8], Larry Vang[2], Taylor Barongan[2], Heather K. Beasley[2,9], Taylor Rodman[2], Margaret Mungai[10], Marcelo Correia[11], Vernat Exil[12], Sandra A. Murray[13], Jeffrey L. Salisbury[5], Brian Glancy[14,15], Renata O. Pereira[11,16#], E. Dale Abel[11,16#], and Antentor O. Hinton Jr.[2#]

[1] Department of Biology, University of Hawaii at Hilo, Hilo, HI

[2] Department of Molecular Physiology and Biophysics, Vanderbilt University, Nashville, TN

[3] National Heart, Lung, and Blood Institute, National Institutes of Health, Bethesda, MD

[4] Central Microscopy Research Facility, University of Iowa, Iowa City, IA

[5] Microscopy and Cell Analysis Core Facility, Mayo Clinic, Rochester, MN

[6] Department of Neurobiology, Harvard Medical School, Boston, MA

[7] School of Medicine, University of Utah, Salt Lake City, UT

[8] Eastern Region, King Abdullah International Medical Research Center, King Saud bin Abdulaziz University for Health Sciences, Al Hasa, Saudi Arabia

[9] Department of Biochemistry, Cancer Biology, Neuroscience and Pharmacology, School of Graduate Studies and Research, Meharry Medical College, Nashville, TN 37208, USA

[10] Department of Molecular and Cell Biology, University of California Berkeley, Berkeley, CA

[11] Department of Internal Medicine, University of Iowa Carver College of Medicine, Iowa City, IA

[12] Department of Pediatrics, Carver College of Medicine, University of Iowa, Iowa City, IA

[13] Department of Cell Biology, School of Medicine, University of Pittsburgh, Pittsburgh, PA

[14] National Institute of Arthritis and Musculoskeletal and Skin Diseases, National Institutes of Health, Bethesda, MD

[15] National Heart, Lung, and Blood Institute, National Institutes of Health, Bethesda, MD

[16] Fraternal Order of Eagles Diabetes Research Center, Iowa City, IA

[†]These authors share first authorship.

#These authors share senior authorship.

*** Correspondence:**
Antentor O. Hinton, Jr
antentor.o.hinton.jr@Vanderbilt.Edu

Keywords: autophagosomes, lysosomes, transmission electron microscopy, autophagy, 3D Reconstruction, DRP-1, MFN-2.

Abstract

Many interconnected degradation machineries including autophagosomes, lysosomes, and endosomes work in tandem to conduct autophagy, an intracellular degradation system that is crucial for cellular homeostasis. Altered autophagy contributes to the pathophysiology of various diseases, including cancers and metabolic diseases. Although many studies have investigated autophagy to elucidate disease pathogenesis, identification of specific components of the autophagy machinery has been challenging. The goal of this paper is to describe an approach to reproducibly identify and distinguish subcellular structures involved in macro autophagy. We provide methods that help avoid common pitfalls, including a detailed explanation for distinguishing lysosomes and lipid droplets and discuss differences between autophagosomes and inclusion bodies. These methods are based on using transmission electron microscopy (TEM), capable of generating nanometer-scale micrographs of cellular degradation components in a fixed sample. We also utilize serial block face-scanning electron microscopy (SBF-SEM) to offer a protocol for visualizing 3D morphology of degradation machinery. In addition to TEM and 3D reconstruction, we discuss other imaging techniques, such as immunofluorescence and immunogold labeling that can be utilized to reliably and accurately classify cellular organelles. Our results show how these methods may be used to accurately quantify the cellular degradation machinery under various conditions, such as treatment with the endoplasmic reticulum stressor thapsigargin or ablation of the dynamin-related protein 1.

1 Introduction

Macroautophagy, the mechanism by which intracellular components or damaged organelles are removed and degraded to maintain cellular homeostasis [1], has much relevance in the fields of disease research and drug development. Although poorly understood, autophagy regulation is broadly implicated in disease pathogenesis, with both overactive and underactive autophagy having negative consequences, including malignant transformation and cellular proliferation in cancer or accumulation of ineffective cells in neurodegenerative diseases [2,3]. Autophagic processes differ depending on their activation pathways, being either non-selective or selective for specific cellular organelles or proteins [1,2]. Growing interest in neurodegenerative and other diseases with autophagy implications has highlighted its consequential roles in key biological processes [1,4].

The complex, regulated macro autophagic process involves structures that also contribute to the cellular recycling machinery specifically, autophagosomes and lysosomes (Figure 1A). The main stages of autophagy include initiation, elongation, autophagosome formation, autophagosome recruitment and maturation, fusion, and degradation [1–3]. In the initiation stage, often triggered by amino acid starvation, sack-like autophagosome precursors, called phagophores, assemble adjacently to the endoplasmic reticulum, typically at mitochondria-associated endoplasmic reticulum (ER) membrane (MAM) (Figure 1B) [5]. The phagophore resides proximal to the ER as an empty, unclosed membrane. As materials are delivered to the phagophore, the membrane closes to seal the organelle, transforming the phagophore into an autophagosome, which carries cytoplasmic components, cargo proteins or organelles designated for degradation. In many cases, the

autophagosome then ultimately fuses with a lysosome, containing hydrolases and permeases, to form an autolysosome and initiate degradation (Figure 1B). In some cases, the autophagosome may mature through an intermediate prior to lysosome fusion known as an amphisome [6]. Importantly, this endosome fusion event may occur to allow for retrograde transport motility, so amphisomes can move to lysosome dense areas [6,7]. In either case, after autolysosome formation, the resulting macromolecules are released through permeases and the ultimate fate of autolysosomes following this process is still unclear [8]. Some autolysosome components can be used to reform lysosomes or become part of new phagophore membranes. Macromolecules released into the cytosol are recycled for use in other biological functions [1–3,9].

Transmission electron microscopy (TEM) has advanced autophagy research by enabling the study of subcellular components at high resolution [4]. By transmitting electrons through ultrathin sections of fixed and embedded samples, TEM generates nanometer-scale micrographs that allow study of autophagic processes [10–12]. For example, past studies have utilized TEM to show autophagosome formation at MAMs and have delineated the maturation process described above [10,12]. Our method uses the free, open-source ImageJ software platform to analyze TEM micrographs of autophagic components [13], enabling image quantitation and statistical analysis [11]. Here we applied this established TEM method recently described by Lam et al. [11] to analyze mitochondria and ER.

While TEM is powerful for identification, it only allows for two-dimensional (2D) visualization of organelles. This may not always be an accurate representation since organelles are three-dimensional (3D) objects. Therefore, we also included reconstrucions from serial block face-scanning electron microscopy (SBF-SEM) [14], which functions by slicing a sample in the z-axis to obtain orthoslices [15]. These orthoslices can then be hand-segmented, one-by-one, to allow for the 3D rendereings of an organelle to be evaluated [16]. While this allows for more accurate representation, there is a much larger time and cost associated with it than TEM quantification. Here we also utilized an established SBF-SEM method recently described by Garza-Lopez et al. [16], to perform 3D reconstruction of recycling machinery organelle alongside TEM quantifications.

The success of our modified protocol depends on proper identification of cellular degradation components. In Figure 1, we showcase how typical organelles should appear conventionally: lysosomes (Figure 1C, red arrows), autolysosomes (Figure 1C-D, blue arrows), golgi (Figure 1C-D, dark blue arrow), autophagosome (Figure 1D, green arrow), early endosome (Figure 1D, black arrow), late endosome (Figure 1D, black outlined white arrow) and lipid droplets (Figure 1E, orange arrow). However, identification is complicated by diverse morphologies with recycling machinery sometimes not presenting typical presentation. For example, lysosomes are usually depicted as spherical, typically ranging from 0.2 to 0.5 micrometers in diameter, although they can also commonly present from 0.05 to 1 micrometers (Figure 2A–D; Table 1) [17–19]. Lysosomes are typically transported by microtubules to the region around the microtubule-organizing center [20]; however, intracellular conditions, such as raised pH, cause lysosomes to migrate toward the cell membrane [21]. Lysosomes are classified as primary, secondary, or tertiary, depending on their digestive activities and their formation process. Lysosome identification is further complicated by their tendency to feature multiple membranes [22]. In quantifying lysosomes, researchers must avoid misidentifying them as multilamellar vesicles, also identified as late endosomes or multilamellar bodies (MLBs; Figure 2E–F; Table 1), which contain lipids within a central compartment surrounded by many membrane bilayers [23]. Lysosomes should not be mistaken for multi-inclusion bodies and multivesicular bodies (MVBs), also known as pre-vacuolar compartments, that are an intermediary structure between vacuoles and the *trans*-Golgi network (Table 1) [24]. Although these structures are

related to autophagy, they differ from lysosomes and autophagosomes and should be excluded from both their quantifications [25]. Lysosomal membranes have highly organized inner folds and lysosomal enzymes have a distinct, darker, and more consistent appearance than the lipids found in MLBs (Figure 2A–F; Table 1). MLB lipids can also appear as dots that speckle the MLB interior, which can be used to differentiate MLBs from lysosomes, although these dots can also be mistaken for cargo in secondary lysosomes (Figure 1A-C; Table 1). Despite these considerations, accurate and reproducible lysosome identification based solely on TEM imaging may be inconsistent, necessitating use of imaging techniques, such as fluorescent staining. Not only do we need to positively identify lysosomes, but autophagosomes must be identified, characterized, and distinguished from lysosomes and other structures.

Autophagosome appearance can also vary depending on the cargo, further complicating their identification (Figure 2G-H; Table 1). Autophagosomes typically have clear double-limiting membranes that appear darker than the rest of the TEM image, separated by a small electron lucent space. However, autophagosomes may also appear with a single membrane or with several separate membranes due to fixation techniques (Figure 2G-H; Table 1) [26]. These diverse membrane presentations can cause misidentification of malformed mitochondria or ring-shaped ER as autophagosomes. Because MVBs and MLBs only display a single membrane (Figure 2E-F; Table 1), presence of a second membrane, in addition to inner recycled ribosomes, more circular shapes representing cargo, or more internal lipids, all characterize autophagosomes (Figure 2G-H). [23,26]. However, improper fixation techniques may cause one of autophagosome limiting membranes to be invisible [26]. MVBs are also generally smaller than autophagosomes and lysosomes, whereas MLBs are larger, sometimes up to ten times the size of typical lysosomes [17,23]. During identification, certain autophagosome types can be included or excluded. For example, if structures appear empty or lacking material, they are likely not involved in degradation and may be excluded. For example, in some disease states, autophagosomes may dysfunction in cargo recruitment and are known as “empty” autophagosomes [27]. Therefore, a key trait of autophagosomes is the presence of cargo. However, it is important to avoid classifying empty autophagosomes as lipid droplets (LDs; Figure 2I–K; Table 1). Similarly, if the body of a phagophore that has not yet closed (Figure 1B) to form an autophagosome, it should not be mistaken as an autophagosome [4,26]. Autophagosomes that are in the process of fusing with a lysosome, also known as lipofuscin granules (Figure 2C, 2E-D), but are not yet considered autolysosomes, can be classified as autophagosome-lysosome fusions, and be considered autolysosomes if their inclusion is consistent [1,2,28]. Since they, physiologically, are similar to autolysosomes, our criteria includes them in autolysosome quantifications [29]. These intermediate structures are identified by their much larger appearance, and contents of the lysosome and the autophagosome often appear to be interacting (Figure 2C, 2E-D).

Autophagosomes that contain limited cargo volumes (Table 1) can mimic large, irregularly-shaped lysosomes (Figure 2A; Table 1) [1,17]. Although autophagosomes can mainly be identified by two limiting membranes, because lipids are not reliably preserved during sample preparation, limiting membranes may vary in appearance, furthering potential for confusion [26]. Another key to identifying autophagosomes formed from non-selective phagophores is recognizing nearby cytoplasmic content inside of them; often autophagosomes can be identified by presenting cargo originating from cytoplasmic content nearby the organelle [30,31]. Furthermore, autolysosomes can differ in their presentation (Figure 2B-C, 2J-O), especially lipofuscin granule autolysosomes (Figure 2C, E-D; Table 1) which may be mistaken for LDs (Figure 2I-J; Table 1) or lysosomes (Figure 2A–D; Table 1). Careful consideration of these features is essential to properly identify these organelles.

Ultrastructural characteristics of organelles can be used to distinguish them from autophagic components. For example, the presence of regularly-spaced ribosomes, which typically appear as small black dots, or a thinner width wrapped around organelles such as mitochondria, strongly indicate that the structure is ER. Similarly, evidence of mitochondrial cristae or inner membrane folds can be used to identify mitochondrial structures. However, exact identification of specific organelles can be complicated. For example, partially degraded ribosomes can aggregate in autophagosomes, forming electron dense clumps as they degrade [26]. However, the presence of ribosomes alone does not confirm an object is an autophagosome, as it is possible to mistake circular cisterns of rough ER for autophagosomes [26]. Autophagosomes may be distinguished by their more circular presentation and higher-degree of clumped ribosomes [12,26].

Although basic processes of autophagosome formation are understood, specific pathways and degradation machinery require further study, such as lipid mobilization from LDs to provide energy. Like all organelles, LDs are targeted by autophagy for recycling and interestingly, macromolecules released by autophagy can be stored in new LDs, even under starvation conditions [32]. Thus, a consequence of autophagy is increased LDs within a cell. These lipid droplets can protect against ER stress and may protect against mitochondrial autophagy, known as mitophagy, by forming close mitochondria-to-lipid contacts [33]. Autophagy impacts nearly every cellular organelle due to its role in organelle degradation. For example, ER stress can initiate autophagy to recycle damaged ER membranes, contributing to healthy ER [34]. Similarly, impaired mitochondrial fission or other l dysfunctions due, for example, to impaired function of critical regulatory proteins, such as mitofusin 1 (MFN1), can trigger mitophagy to clear ineffective mitochondria [35,36]. Because all organelles interact with the cellular degradation machinery, understanding the dynamics between primary recycling organelles—lysosomes, autophagosomes, and autolysosomes—and other organelles is critical to fully appreciate the contributions and drivers of autophagy. Careful and accurate identification of components of the autophagy machinery are needed to advance our understanding of therapeutic effectiveness, whose mechanisms of action may involve autophagy. This effort may elucidate additional pathways that induce autophagy and clarify how autophagy contributes to disease prevention and progression [37]. Accurate characterization and quantitation of autophagy components requires proper identification of these degradation organelles and other subcellular structures involved in autophagic processes.

Although many studies have identified components of autophagosome and lysosome machinery, developing next-generation methods to rigorously identify and quantify these organelles is essential to establish standardized protocols, allowing data comparison [10,26,38–40]. Many of these structures are similar, but can differ from cell to cell and are easily misidentified. A basic understanding of the potential and common appearances of lysosomes and autophagosomes is critical for TEM analysis. Here, we describe characteristics that should be assessed to properly identify autophagic organelles and provide recommendations for effective classification (Supplementary Figure 1).

Our ultimate goal was to identify and quantify difficult-to-measure autophagic machinery in clear terms and present a novel approach to measure all cellular degradation machinery using free, open-source software. These techniques can be used to reproducibly quantify and characterize changes in the organelles associated with autophagy. Furthermore, for researchers who wish to perform more complex calculations and resource-intensive imaging, we also offer a protocol for 3D reconstruction of recycling machinery.

2 Methods and Materials

207 2.1. Mouse Care & Maintenance

208 Mouse husbandry was performed based on prior protocols [41] according to with protocols approved
209 by the University of Iowa Animal Care and Use Committee (IACUC). Male C57Bl/6J mice were
210 housed at 22 °C with a 12-h light, 12-h dark cycle, and free access to water and standard chow. Mice
211 with a tamoxifen-inducible knockout of DRP1 in skeletal muscle were generated by crossing mice
212 carrying a homozygous floxed allele of DRP1 with mice carrying a tamoxifen-inducible Cre
213 recombinase under control of the myogenin promoter (Jackson Lab) in skeletal muscle as previously
214 described [42,43]. Myotubes were isolated from these mice, using protocols described below.

215 2.2. Fly Strains and Genetics:

216 A mitochondrial assembly regulatory factor (Marf) knockdown fly was generated according to
217 previous protocols [44]. Genetic crosses were performed on yeast corn medium at 22 °C. W1118
218 flies were used as genetic background controls. Mef2- Gal4 (III) was used to drive muscle-specific
219 Marf RNAi (BS# 55189) to achieve gene knockdown. Mef2-Gal4 (BS# 27390) stocks were obtained
220 from the Vienna Drosophila Stock Center and Bloomington Drosophila Stock Center. All
221 chromosomes and gene symbols are as mentioned in Flybase (http://flybase.org).

222 2.3. Isolation of Satellite Cells & Differentiation

223 When adopting this protocol, an individual who was blinded to the mouse genotype or treatment
224 conducted the experiment, including isolation, differentiation, and fixation of murine and human
225 cells. This individual did not perform later analyses to mitigate bias. Satellite cell isolation and
226 differentiation for thapsigargin treatment and DRP-1 ablation were performed as described
227 previously, with minor modifications [11,41,45]. When C57B1/J1 mice reached 8–10 weeks of age,
228 mice were anesthetized using isoflurane. Skeletal muscles of the gastrocnemius and quadriceps were
229 excised and washed twice with 1× phosphate-buffered saline (PBS) supplemented with 1%
230 penicillin-streptomycin and 0.3% fungizone (300 µL/100 mL). Dulbecco's modified Eagle's medium
231 (DMEM)-F12 media with 0.2% collagenase II (2 mg/mL), 1% penicillin-streptomycin, and 0.3%
232 fungizone (300 µL/100 mL) was added to the muscles and shaken for 90 min at 37 °C. This media
233 was removed, muscle was washed with PBS x4 times, and media replaced with DMEM-F12 media
234 containing 0.05% collagenase II (0.5 mg/mL), 1% penicillin-streptomycin, and 0.3% fungizone (300
235 µL/100 mL), before shaking for 30 min at 37 °C. Tissue was then ground until all cells were
236 dislodged from the tissue matrix and were passed through a fine, 70-µm cell strainer. Isolated cells
237 were centrifuged, resuspended, and plated on BD Matrigel-coated dishes. Adherent cells were
238 differentiated into myotubes by adding DMEM-F12, 20% fetal bovine serum (FBS), 0.004% (40
239 ng/mL) basic fibroblast growth factor (R&D Systems, 233-FB/CF), 1× non-essential amino acids,
240 0.14 mM β-mercaptoethanol, 1× penicillin/streptomycin, and 0.3% fungizone (300 µL/100mL).
241 Myotubes were maintained in medium containing 0.001% (10 ng/mL) growth factor until reaching
242 85% confluency, then were differentiated in DMEM-F12, 2% FBS, and 1× insulin–transferrin–
243 selenium.

244 2.4. Human Myotubes

245 GIBCO® Human Skeletal Myoblasts from ThermoFisher Scientific (A1255) were thawed and plated
246 in HG DMEM containing 1% penicillin/streptomycin, 1% fungizone, and 2% horse serum. Cells
247 were differentiated after 48 h, and myotubes were extracted.

Fibroblasts grown *in vitro* to the third passage were plated in 6-well tissue culture plates (5×10^5 cells per well) in DMEM (Invitrogen) supplemented with 10% heat-inactivated fetal bovine serum, 100 U/ml penicillin, 100 µg/ml streptomycin, 0.25 µg/ml fungizone, 1 mm sodium pyruvate, and 10 mm HEPES at 37 °C in a humidified incubator with 10% CO_2. Cells were infected with Ad-Cre and Ad-GFP was a control.

2.5 Immunogold Labeling

Immunogold labeling was performed as previously described [46]. Ultrathin cryosections were prepared, and single- or double-immunogold labeling was performed using antibodies and protein A coupled to gold. After labeling, sections were imaged via TEM. Specifically, primary skeletal myotubes were fixed for 1 h in 4% paraformaldehyde (PFA) and 0.1% glutaraldehyde in 0.1 M phosphate buffer. From there, vibratoming of 40-50 µm section into 0.1M phosphate buffer was performed. Each section was washed 3 times for 10 minutes each with the same 0.1 M phosphate buffer. For the first blocking step, 0.1% NaBH4 in 0.1 M phosphate buffer was applied for 15 minutes. After blocking, phosphate buffer was used for washing 4 times for 10 minutes each time. To permeabilize, 0.05% Triton X-100 in 0.1M phosphate buffer was applied and incubated for 15 mins at 30 °C. After this, phosphate buffer was used for washing 3 times for 10 minutes each time. For the second blocking, Aurion Blocking Solution was added and the solution was incubated at room temperature for one hour. Incubation buffer was used to wash after blocking, again in triplicates of 10 minutes.

From there, 1-5 µg/ml of the primary antibody in incubation buffer was applied and incubation at 4 °C occurred overnight. For mitofusin-1, Anti-Mitofusin 1 antibody was used (Abcam; ab126575); for CAV-1, caveolin-1 antibody was used (Cell Signaling Technology; 3238); and for LC3, LC3B (D11) XP® Rabbit mAb was used (Cell Signaling Technology; 3868). After overnight, the incubation buffer was used to rinse 6 times over, incubating for 10 minutes each time. From there, secondary antibody incubation occurred with 1:100 ultrasmall gold conjugated secondary antibody in incubation buffer overnight at 4 °C. After overnight, again the incubation buffer was used to rinse 6 times over, incubating for 10 minutes each time. Furthermore, 3 washes, each 10 minutes, of PBS were also used. From there, post-fixation occurred through incubation in 2% Glutaraldehyde in 0.1M phosphate buffer for 2 hours. After time elapsed, phosphate buffer was utilized for washing across 4 times, 10 minutes each time. It was quickly rinsed with distilled H_2O for 15 seconds, three times. For silver enhancement, AURION SE-EM silver enhancement solution was applied, and sample incubated for 45 minutes at room temperature. From there, it was quickly rinsed with distilled H_2O for 15 seconds, three times. Phosphate buffer was also utilized for washing across 4 times, 10 minutes each time. Once washed, to perform osmification, 0.5% OsO4 in 0.1M phosphate buffer was added for 15 mins. After this, the sample was finally washed in the same phosphate buffer for 10 minutes twice.

From there, dehydration and embedding in resin was performed. To do so, first the sample was again placed in 4% PFA and 0.1% Glutaraldehyde for 1 h. From there, they were washed with phosphate buffer three times for 20 minutes. Following this, a graded ethanol wash was performed at 15 minutes each progressing from 25% to 50% to 75% ethanol. 95% ethanol was finally used for wash for 30 minutes. From there, the mixture was washed and replaced with an 1:1 mixture of 95% ethanol and LR white resin for 1 hr. Finally, a pure 100% LR white resin solution was added. After an hour, it was replaced with a new 100% LR white resin which again incubated at room temperature for 1 hr. This sample was cured under UV overnight with a vacuum to remove any excess liquid. 90 nm ultrathin sections were obtained and imaging occurred as described for TEM samples below.

293

294 2.6 Lysotracker

295 The protocol was performed as previously described [47]. LysoTracker™ Red DND-99
296 (ThermoFisher Scientific, L7528) was diluted to a final concentration of 1 mM with dimethyl
297 sulfoxide (DMSO) to create a stock solution, which was then mixed with warm growth media at a
298 1:2000 dilution. Growth media was aspirated from cells and replaced with the working
299 LysoTracker™ Red DND-99 solution. Cells were imaged live using an SP-8 confocal inverted
300 microscope with a visible light laser at a 577 nm excitation wavelength and a 590 nm ± 10 nm
301 emission wavelength, which allowed a yellowish pseudo coloration to be observed. To stain fixed
302 cells, cells were grown in culture media on a #1.5 cover glass, either embedded into a petri dish or
303 divided by plastic-walled growth chambers to optimize microscope optics. Cells were incubated for
304 30 min with a LysoTracker™ Red DND-99 working solution. The staining solution was then
305 aspirated from the plate, rinsed, and subsequently fixed in 4% PFA. Confocal image stacks were
306 captured with a Zeiss LSM-5, Pascal 5 Axiovert 200 microscope, using LSM 5 version 3.2 image
307 capture and analysis software and a Plan-APOCHROMAT 40x/1.4 Oil DIC objective. Images were
308 deconvoluted with National Institutes of Health (NIH) ImageJ software and BITPLANE-Imaris
309 software. Imaris software analysis was used to measure lysosome number, volume, and area.
310 Experiments were conducted in triplicate, at minimum, and 10–20 cells per condition were
311 quantified.

312 2.7. Immunofluorescence

313 Immunofluorescence was performed as previously described [41,48]. For, live-cell imaging, live cells
314 were plated and imaged in MatTek 35 mm glass-bottom culture dishes and grown on Matrigel. After
315 growth, the cells were fixed with 4% (w/v) PFA in PBS for 30 min, then permeabilized with 0.25%
316 Triton X-100 in PBS for 10 min at room temperature. Fixed cells were then blocked with 10% bovine
317 serum albumin in PBS and incubated with rabbit anti-lysosomal associated membrane protein
318 (LAMP-1; Cell Signal: D2D11) antibody in 1% BSA in PBST (PBS + 0.1% Tween 20) at a 1:25
319 dilution at 4 °C overnight. After three PBS washes, each 5 minutes long, Alexa Fluor 488-conjugated
320 goat-rabbit mouse IgG (Life Technologies: A-11008) secondary antibodies were added at 1:1000
321 dilution in 1% BSA and incubated at room temperature for 45 minutes in the dark. After another
322 three PBS washes, coverslips were mounted onto glass slides with ProLong Diamond Antifade with
323 4',6-diamidino-2-phenylindole (DAPI) and allowed to dry overnight. Confocal image stacks were
324 captured with a Zeiss LSM-5, Pascal 5 Axiovert 200 microscope, using LSM 5 version 3.2 image
325 capture and analysis software and a Plan-APOCHROMAT 40x/1.4 Oil DIC objective. Imaris
326 software analysis was used to measure lysosome intensity, length, and sphericity. Experiments were
327 performed in triplicate, at minimum, and 10–20 cells per condition were quantified.

328 2.8. Thapsigargin Treatment

329 Fibroblasts, human myotubes, and mouse myotubes were treated with thapsigargin (2 μg mL^{-1};
330 Sigma) for 10 h, followed by crosslinking with Trump's fixative [49] with 4% PFA and 1%
331 glutaraldehyde for 10 min as previously described [11,50].

332 2.9. TEM Processing of Myoblasts, Fibroblasts, and Myotubes

333 The cell types followed a near identical procedure. Myoblasts and fibroblasts were isolated according
334 to the above methods and placed in six-well poly-D-lysine–coated plates for TEM processing.

Myotubes were cultured on Matrigel coated plates. For 1h, cells were incubated at 37 °C with 2.5% glutaraldehyde in 0.1 M sodium cacodylate buffer. This resulted in cell fixation. From there, after rinsing twice with 0.1 M sodium cacodylate buffer, secondary fixation at room temperature for 30 minutes to one hour occurred using 1% osmium tetroxide and 1.5% potassium ferrocyanide in 0.1 M sodium cacodylate buffer.

After secondary fixation, a five-minute washing with 0.1 M sodium cacodylate buffer (7.3 pH) occurred. From there, two washings of five minutes with diH_2O ensured the plates were cleaned. While keeping all solutions and plates at room temperature, the plates had 2.5% uranyl acetate, diluted with H_2O, added and were incubated overnight at 4° C. Following this, dehydration was performed though an ethanol gradient series. After dehyrdation, the ethanol was replaced with Eponate 12™ mixed with 100% ethanol in a 1:1 solution. The cells were allowed to incubate, again at room temperature, for 30 minutes. This was repeated three times, for an hour each time using 100% Eponate 12™. The plates were finally placed in new media and placed in an oven overnight at 70 °C.

The plates were cracked upon hardening, and the cells were separated by submerging the plate in liquid nitrogen. An 80nm thickness jeweler's soul was used to cut the block to fit in a Leica UC6 ultramicrotome sample holder. From there, the section was placed on formvar-coated copper grids. These grids were counterstained in 2% uranyl acetate for 2 minutes. Then these grids were counterstained by Reynold's lead citrate for 2 minutes. Images were acquired by TEM on either a JEOL JEM-1230, operating at 120 kV, or a JEOL 1400, operating at 80kV.

2.10. Systematic ImageJ Parameters and Measurement

Using documented parameters and quantification methods [11], a unique individual imaged the entire cell at low magnification. Obtained images were uploaded to ImageJ in an acceptable format, such as TIFF. The cell was then divided into quadrants using the ImageJ quadrant picking plugin (*https://imagej.nih.gov/ij/plugins/quadrant-picking/index.html*, accessed August 21, 2021) to ensure random and unbiased quadrant selection for quantification. After sectioning the image into four quadrants, two quadrants were randomly selected for complete analysis. Three independent, blinded individuals quantified these quadrants as described below. Their collective findings were averaged to decrease individual subjective bias. To ensure accurate and reproducible values, measurements were repeated on a minimum of 10 cells each. In the future, if significant variability is observed among the individuals performing the analysis, increasing the sample number (n) by expanding the number of cells quantified was found to decrease variability.

All analysis methods were developed using NIH ImageJ software. Necessary measures should be set on ImageJ prior to analysis (Analyze > Set Measurements: Area, Mean gray value, Min & Max gray value, Shape descriptors, integrated density, Perimeter, Fit ellipse, Feret's Diameter). Lysosomes, autolysosomes, LDs, and autophagosomes, were measured, including area, circularity, and length using the Multi-Measure region of interest (ROI) tool in ImageJ based on established measurements [11,51]. Using the freehand tool in NIH ImageJ 1.49, we manually traced the cellular degradation machinery membrane to determine area or volume. A 19 × 23 cm rectangular grid was overlaid on each image to quantify cellular degradation structures and the numbers were presented per 10 μm^2 of cytoplasm.

2.11. Statistical Analysis

Results are presented as the mean ± standard error of the mean. Data were analyzed using unpaired Student's T-tests. If more than two groups were compared, one-way analysis of variance (ANOVA) was performed, and significance was assessed using Fisher's protected least significance difference test. For T-tests and ANOVA, the GraphPad and Statplus software packages were used (SAS Institute, Cary, NC). For all statistical analyses, significant differences were accepted when $p < 0.05$.

2.12 3D reconstruction of cellular degradation components using Amira

Following isolation of myotubes in a flex fixative, serial block face-scanning electron micrscopy was performed according to established protocols [16]. Once isolated, *Amira* 3D reconstruction (ThermoFisher Scientific; Waltham, Massachusetts) software was utilized to perform 3D reconstruction of machinery according to the protocol found in Section 3. All videos were created in the *Amira* software program according to Garza-Lopez et al. 2022 [16].

3 Protocol

TEM PROTOCOL:

3.1. Downloading and Preparing ImageJ Software for Analysis

3.1.1. Download ImageJ software from the official NIH website (https://imagej.nih.gov/ij/download.html).

3.1.2. Install and open the ImageJ software.

3.1.3. Select Analyze ▸ Tools ▸ ROI Manager to open the ROI Manager, which is used to record and track measurements.

3.1.4. Click on Analyze ▸ Set Measurements to input the measurements for ImageJ to perform, such as area, circularity, and perimeter.

3.1.4.1. For the current protocol, area and count were the focus; however, all available measurements may be used, depending on the study aims.

3.1.5. Import image to be analyzed directly into ImageJ. A TIFF or DM3 file is recommended to provide high-quality.

3.1.5.1. Alternatively, click File ▸ Open to open the selected image.

3.1.6. Considerations

3.1.6.1. For accuracy and reproducibility, ensure that each image contains a scale bar, bar length, and image magnification. The scale bar and bar length are important for setting the appropriate units in the ImageJ settings.

3.1.6.2 Quantification of samples should be performed by three individuals in a randomized and blinded manner to ensure an unbiased approach.

3.1.6.3. To save time, images may be divided into quadrants, and same quadrants should be analyzed across all images.

3.2. Analyzing Lysosomes, Autophagosomes, and Autolysosomes (Supplementary Figure 2A–C)

3.2.1. Click on Freehand Selections to access the Freehand tool.

3.2.2. Trace the outline of the entire cell.

3.2.3. Click Add on the ROI Manager. This ROI will be used to normalize later measurements.

3.2.4. To obtain length and width, use the Straight-Line tool to draw a line down the major and minor axes of each organelle (Supplementary Figure 2A–C, Step 1).

3.2.5. Trace the membrane of each lysosome, autophagosome, or autolysosome. Add the shape to the ROI Manager (Supplementary Figure 2A–C, Step 2).

3.2.6. Click Measure in the ROI Manager to obtain the area measurements.

3.2.7. Add the measurements to the ROI Manager and use the Measure function to obtain numerical values for each measurement.

3.2.8. Considerations

3.2.8.1. Ensure that autophagosomes, lysosomes, and autolysosomes are measured separately because the ROI Manager will group all functions for statistical analysis.

3.2.8.2. The number of autophagosomes, lysosomes, or autolysosomes counted in the cell should be normalized against the total cell area.

3.3. Analyzing Lipid Droplets

3.3.1. Repeat Steps 2.1–2.5 for LDs to obtain basic measurements needed for analysis (Supplementary Figure 2D).

3.3.2. For each cell, calculate total area of all LDs. The amount of lipid coverage is the total area of all LDs divided by total cell area.

3.3.2.1. This process can be used to determine the percent coverage of other subcellular structures, including mitochondria and recycling machinery.

3.3.3. Contact sites between organelles can be measured by first using the Freehand tool to trace the outer membranes of both subcellular structures being analyzed, as described in Step 2.4 (Supplementary Figure 2D, Step 1).

3.3.4. To determine the contact site length, click on the Straight, Segmented, or Freehand Lines tool on the toolbar, and select Freehand Line. Draw a line spanning the length of the contact site, add the measurement to the ROI Manager, and use the Measure function to determine the contact length (Supplementary Figure 2D, Step 2).

3.3.5. Contact distance may be similarly measured using the Freehand Line tool to draw a line between two objects being measured.

3.3.6. Calculate percent coverage by dividing the cumulative contact lengths by the percent coverage of one of the two subcellular features in question, as determined in Step 3.2. Multiply the value by 100 to obtain a percentage.

3D RECONSTRUCTION PROTOCOL (UTILIZING WACOM TABLET):

3.A. Download Amira software from https://www.thermofisher.com/us/en/home/industrial/electron-microscopy/electron-microscopy-instruments-workflow-solutions/3d-visualization-analysis-software/amira-life-sciences-biomedical.html (accessed on 4 August 2022) and open.

3.B. Transfer all orthoslices to be analyzed from **Project View > Open Data.** Ensure all are transferred by selecting **Read Complete Volume into Memory**.
3.C. Navigate between the **Project** subsection, to select images to analyze and the the **Segmentation** subsection, to alter segmentation tools. We recommend the **Brush** tool with a size of 2.

3.D. Calibrate the Wacom Pen and open Amira on the Wacom tablet in accordance with prior protocols [16].

3.E. Using arrow keys, scroll through orthoslices until desired recycling machinery is found. It is recommended to verify its identity by looking at additional orthoslices. For each organelle, outline with a material and press F to segment area. Alter material for each organelle to pseudo color organelles.

3.F. Repeat this process for each ortho slice that organelle appears on, making sure that all independent organelles consistently use the same material color. Later on, aspects of these materials, such as color and visibility, can be altered on the **Materials** menu.

3.G. Once all are segmented, on the **Project Menu**, click on **Selection Labels > Generate Surface** and select **Apply**.

3.H. In the workplace area of Amira, rename the newly generated box with the "**. surf**" suffix and click **Surface View**. Toggle orthoslice and 3D reconstruction materials on and off to switch between isolated and overlay view.

3.I. Make scale bars by right-clicking in the gray area under the **Project** subsection and selecting the option **Scalebars**. Adjust scale bars as necessary, with a readable width and font, as well as only leaving x-axis, unless y-axis scale is also necessary.

3.J. Previously [16], mitochondrial quantifications performed has included volume, 3D area, and length. Furthermore, mitochondrial complexity index is measured by $SA^3/16pi^2V^2$ while mitochondrial branching index measures transverse branching divided by longitudinal branching [52]. While created for mitochondria, these same quantifications can be used as parameters for recycling machinery. Additionally, recycling machinery has other quantifications that may be applied including mitochondrial-lysosome or lipid droplet-mitochondrial interactions distances and surface area interactions.

4 Result

This protocol describes a method to obtain reproducible measurements and identify structures involved in autophagy. Below, we show the results obtained using this TEM image analysis approach.

4.1. Identification of organelle compartments by immunogold labeling

With the pitfalls associated with correctly identifying organelles by TEM morphology alone, other methods may be required to confirm organelle identity. One of the most effective alternatives is immunogold labeling used in electron microscopy to analyze organelle marker proteins. As a positive-control, it is useful to perform immunogold labeling on a easily identifiable organelle. For example, mitochondrial GTPase proteins, mitofusin 1 and 2 (MFN1 and MFN2), function in mitochondrial fusion reactions [35,36,53–56] and MFN1 is used to identify mitochondria in tissues as MFN1-positive puncta (Figure 2P–Q).

Immunogold labeling can also be used to identify organelles associated with autophagy. Many novel yeast genes that are essential for autophagy (autophagy-related, or ATG genes) have been characterized, and most of their mammalian homologs have been identified [57]. Microtubule-associated protein 1 light chain 3 (LC3), the mammalian homolog of Atg8 [58], is a reliable marker for mammalian autophagosomes, which can be identified by the formation of LC3 labeling along the limited membrane (Figure 2R–S). LC3 expression in autophagosomes (Figure 1, blue arrows) and phagophores (not shown) may vary due to LC3 degradation by lysosomal hydrolases, making it a challenge to identify late-stage autophagic materials [59]. Moreso, since autophagosomes are three-dimensional organelles and are being imaged in two-dimensions. However, identifying LC3-positive puncta is still valuable to identify autophagosomes. Immunogold labeling has also been performed with caveolin-1 (CAV-1), a marker protein for specialized membrane domains known as caveolae, which ultimately accumulate in caveosomes that mature into MVBs upon endocytosis [60]. Therefore, CAV-1 immunogold labeling can be used to identify vesicles (Figure 2T–U) and the presence of CAV-1 puncta in an ROI excludes those vesicles from classification as autophagosomes, indicating instead a vesicle such as, multivesicular or multi-inclusion body. After testing immunogold labeling, we examined changes in cellular degradation machinery under other conditions.

4.2. Thapsigargin treatment alters lysosome, autolysosome, and autophagosome morphology

Thapsigargin is a sarcoplasmic-ER Ca^{2+}-ATPase (SERCA) inhibitor, that decreases the length of mitochondria–ER contacts in treated cells, while also inducing ER stress [11,61]. We investigated morphological changes in lysosomes, autolysosomes, and autophagosomes in response to thapsigargin (Figure 3) using our TEM image analysis protocol. We found that mean lysosomal area and the number of lysosomes per square micron significantly increased in response to thapsigargin treatment in primary mouse skeletal myotubes (Figure 3E–F). The mean area of autolysosomes and the number of autolysosomes per square micron had an even greater increase than seen in lysosomes (Figure 3G–H). The mean autophagosomal area and number of autophagosomes per square micron also significantly increased in thapsigargin-treated cells (Figure 3I–J). Similar results were seen in mouse fibroblasts (Figure 3K–T) and human myotubes (Figure 3U–AD). Human myotubes displayed the largest increases in autophagy recycling machinery of all assessed components. These quantifications are shown with representative images for each cell type (Figure 3A–D, K–N, and U–X). The ability of thapsigargin to inhibit ER function and promote cell stress support a model in which cell-stress-induced organellar damage increases lysosome and autophagosome degradation of

damaged organelles. Thus, morphological changes detected and quantified using our TEM method are consistent with the expected effects of thapsigargin treatment.

4.3. DRP-1 ablation results in increased degradation machinery

Dynamin-related protein (DRP-1) is a crucial regulator of mitochondrial fission [43,62]. Previous studies found that impaired mitochondrial fission can have downstream effects on organellar morphology and function throughout the cell [63]. In the absence of DRP1, mitochondria undergo fission less frequently, resulting in longer mitochondria that can trigger downstream effects, including apoptosis [62]. To test our method, we generated a skeletal muscle-specific *Drp1* knockout mouse and noted changes in the degradation machinery. Specifically, our study focused on lysosomes, autophagosomes, and LDs, which are all closely linked to the autophagy process. *Drp1* ablation in a skeletal myotube-specific knockout model (DRP-1smKO), resulted in significantly more lysosomes than in wild-type controls (Figure 4A–F, red arrows). We also found increased lysosome numbers per square micron and lysosomal area per square micron, although the change in lysosomal area was not as great as the change in lysosome number (Figure 4G–H). Similarly, DRP-1smKO also showed a significant and large increase in autophagosome number over wild-type controls (Figure 4I–L, red arrows). We also observed increased autophagosome number per square micron and autophagosome area per square micron, although the change in area was less than the change in number (Figure 4M–N). Based on changes in percentage and degree of significance, the autophagosome increase was greater than the lysosome increase, suggesting that reduced mitochondrial fission may cause larger shifts in cargo vessel formation than in lysosome formation, although both organelle types increased significantly. Autophagosome-lysosome fusion events may also contribute to this disparity, as intermediate fusion phase structures more closely resemble autophagosomes than lysosomes.

To validate these results, we used the fluorescent dye, LysoTracker, to image lysosomes in DRP-1smKO myotubes because its ability to label and track acidic organelles in live cells allows it to effectively identify highly acidic lysosomes. Similar to TEM data, the LysoTracker assay showed significantly more lysosomes in DRP-1smKO myotubes than in wild-type controls (Figure 4O-P). Increased lysosome number, calculated lysosome volume, and lysosomal area were also observed in DRP-1 knockout mice (Figure 4Q–S). These key quantitations are similar to those determined by TEM analysis; however, LysoTracker provided better certainty of lysosome identity and allowed use of traditional statistical analyses to determine lysosome area and numbers. Lysosomes can also be identified by LAMP1 immunostaining (Figure 4T–U) [64], which correlates with the number and size of active lysosomes (Figure 4V). While relative intensity can estimate LAMP1 expression, lysosome area measurements are not reliable by LAMP staining. Other metrics, including length and sphericity, can be determined using these fluorescent dyes, suggesting that lysosomal dysfunction occurs as length increases and sphericity decreases (Figure 4W–X).

To further validate these results and see if the 3D structures of recycling machinery showed significant differences upon loss of DRP-1, we also provide representative 3D reconstruction of both lysosomes (Figure 4Y-AB’’; SV1-4) and autophagosomes (Figure 4AC-AF’’; SV 5-8). The top image shows a representative orthoslice of the region of interest (Figure 4Y-AF). Once segmentation was performed, organelle 3D reconstructions were overlaid on the orthoslice (Figure 4Y’-AF’). To allow for better visualization, we also show isolated 3D reconstruction on the X- by Z- plane to allow for their depth to better be visualized (Figure 4Y’’-AF’’). However, static images of 3D reconstruction may not capture the scope of 3D reconstruction; therefore, we also provide associated videos showing organelles for all representative images (SV 1-8). Our study shows that lysosomes

appear larger in DRP-1 smKO (Figure 4AB''). Additionally, upon loss of DRP-1 lysosomes appear to be closer together in 3-dimensional spatial orientation (Figure 4AA''-AB''). Autophagosomes appear to have a less significant alteration, but they do appear to be more elongated in the z-axis upon DRP-1 smKO (Figure 4AC''-AF''), a detail that would otherwise not be observed in TEM.

4.4. DRP-1 ablation results in increased lipid droplets

We also measured LDs in skeletal muscle from DRP-1smKO mice, which had significantly more LDs than WT controls (Figure 5A–B, red arrows). We observed a large increase in lipid area and number of LDs per square micron (Figure 5C–D). Based on percent change, the LD increase was larger than the observed increases in both lysosomes and autophagosomes following DRP-1 ablation (Figures 4 and 5). To see if spatial relationships of LDs changed upon DRP-1 loss, we also looked at SBF-SEM 3D reconstruction of LDs. For both WT and DRP-1smKO mice we show a representative x- by y-plane orthoslice (Figure 5E-H), 3D reconstruction overlaid on orthoslice (Figure 5E'-H'), isolated 3D reconstruction showed on a slightly different plane, the X- by Z-plane, to allow for depth to better be visualized (Figure 5E''-H''), and video of isolated 3D reconstruction (SV 9-12). We observed that after DRP-1 loss, LDs were much more clumped, both on the x- and y- axis, but also on the z-axis, and lipid droplets appeared to be larger sizes (Figure 5G''-H'').

4.5. Knockdown of Marf resulted in more abundant lysosomes

In addition to DRP-1, we sought the quantify lysosomal changes in response to knockdown of other key mitochondrial proteins. Mfn2 is an important regulator of mitochondrial fusion [65,66] and Mfn2 deficiency has been associated with disrupted ER morphology and mitochondria–ER contacts, resulting in dysfunctional calcium signaling [65,66]. Loss of Mfn2 was also recently shown to influence autophagic pathways [65–68] by stalling autophagy at the lysosome and autophagosome stages, causing a buildup of both autophagosomes and lysosomes by inhibiting their fusion [68]. The *Drosophila* homolog of Mfn2 is Marf, and knockout of genes upstream of Marf had downstream effects on autophagy [67]. Given this emerging link between autophagy and Marf/Mfn2, we examined the effects of Marf knockdown in *Drosophila* tissue, which produced a significant and large increase in lysosome number compared with WT controls (Figure 6A–B, D). We also observed an increase in average lysosomal area (Figure 6C). These findings indicate a potential upregulation of autophagy, which may represent an autophagic response to ER and mitochondrial stress caused by loss of Marf [65–68]. Further research into changes in other cellular degradation machinery following loss of Mfn2/Marf could better elucidate the effects of Mfn2/Marf on autophagy.

5 Discussion

The method we have described involves measuring organelles in each image or image quadrant by defining the area of interest using digital tools, rather than the often-used method of point counting. Point counting can be used to determine the cellular area by laying a grid over the cellular area and determining the distance between gridlines and the number of grid intersections, or points, within the cell. Cellular area may then be estimated using the equation $P \times d^2$, where p is the number of points and d is the grid distance [40]. Smaller grids can be used to repeat the process for estimating organelle area, and these two values can then be used to determine the percent coverage of organelles. Past studies have used point counting to successfully streamline the process of calculating organelle coverage; however, this method only provides estimations [40]. Even with smaller grid distances, which can increase the calculation accuracy, this approach still requires estimation. The method we described uses ImageJ to more precisely calculate the structure areas. Although using

ImageJ is more time-consuming, the results are highly reproducible, generating high-quality data that may be further analyzed using ImageJ. Both analyses require human evaluation and proper identification of the recycling machinery. Both point counting and ImageJ-based measurements are viable ways to measure the frequency of recycling or other types of organelles; however, we believe the accuracy of measurements with ImageJ analysis is worth the increased time commitment [23,24].

An important consideration in the use of TEM is the magnification and scope of cellular degradation machinery components to be considered in these analyses. Significant size heterogeneity is seen among components of the degradation machinery, even within the same classification group, which can vary according to the amount of cargo they carry (Figure 1). For TEM imaging, various organelle types and sizes may require different magnifications (Supplemental Figure 1). Additionally, the purpose of the analysis must be considered when deciding which types of recycling machinery to evaluate, and appropriate statistical analyses should be used (Supplemental Figure 1). For example, the total number of LDs may not be as important as their total cell coverage due to varying LD sizes and proper magnification should be determined based on the necessary measurements to be performed (Supplemental Figure 1). A limitation of our method is that for key measurements, such as area, the total organelle must be visualized to obtain accurate results. Point counting can be used to evaluate images in which the entire organelle is not visible because it relies on estimation [40]. When using ImageJ, the entire organelle is outlined, and magnification that is too high may limit the amount of data that can be collected. However, images of a single cell at varying magnifications may be used by normalizing to a consistent scale across all images.

Although this protocol focuses primarily on evaluation of the degradation machinery, these organelles must not be viewed in a vacuum. Autophagy can target any cell, and many factors can alter autophagy processes in different cells, as seen in cancer, metabolic diseases, or neurodegenerative diseases [1,4,12]. Many organelles are closely associated with the overall autophagy process. Recent research found that omegasomes and autophagosomes primarily form at mitochondria–ER contact sites [39], which may be because the ER phospholipid, phosphatidylinositol 3-phosphate, is needed to activate and form autophagosomes [1–3]. Mitochondrial-derived vesicles can also influence autophagic pathways by transporting proteins and lipids associated with the mitochondria to MVBs [69]. This previously unknown pathway indicates that mitochondria that are not sufficiently damaged to trigger mitophagy can still produce endocytic bundles that are transported to the MVB for recycling via the autophagic pathway. Because cellular degradation machinery can have important effects on organelles, and the inverse is also true, a holistic view is needed to understand the nuances that influence autophagy.

The protocol described here is optimized for statistical analyses; however, it is important to ensure that correct subcellular features of lysosomes, autophagosomes, and LDs are identified and measured. Although organelles can be accurately identified by TEM alone, methods, such as immunofluorescent staining, are recommended in tandem with TEM to achieve clear results, particularly when analyzing lysosomes, autophagosomes, and autolysosomes, which are easily misidentified (Figures 1-2 and 4). Because examining organellar morphology using TEM alone may lead to inaccurate conclusions, we suggest coupling TEM with methods such as immuno-TEM with gold labeling, LysoTracker with correlative light and electron microscopy, and immunohistochemistry or immunofluorescence (Figure 2 and 4) to verify the identity of each structure [5,57,70].

Given the acidity and multitude of proteins associated with lysosomes, there are various ways to identify lysosomes using immunogold labeling, LysoTracker to identify acidic organelles,

immunofluorescent dyes to label lysosome-associated proteins such as LAMP1(Figure 4T–U) [64], and indirect immunofluorescence using secondary antibodies bound to a lysosome-associated primary antibody [71,72]. When combining confocal fluorescence imaging and TEM, fluorescence can be used to identify specific proteins and confirm the identities of autophagic organelles (Figure 4O–X), and TEM can be used to measure finer details, including area, average number, and percent coverage (Figure 4A–N). SBF-SEM can from there allow for 3D visualizations and to see details that may not be seen in the 2D plane (Figure 4Y''-AF''; Figure 5E''-H''; SV 1-12). 3D reconstruction can importantly allow for visualization of how organelles exist in relation to each other in a 3D spatial orientation as well as if there is alterations in specifically transverse or longitudinal organelle volumes [16].

Current options to identify and classify autophagosomes are limited. Immunogold labeling can be used to detect LC3, which is currently a commonly used autophagosomal marker that proved effective for our research [57,70,73]. LC3 puncta are not always detectable in autophagosomes; however, immunogold labeling can be used to identify organelles to be excluded from autophagosomes analysis. For example, CAV-1 staining (Figure 2T–U), which is associated with caveolae typically found in MVBs, can identify MVBs that might be mistaken for autophagosomes (Figure 2) [60]. Similarly, perilipin 2, a commonly expressed protein associated principally with LDs, can be used to identify LDs [74]. Future studies that explore new improved immunogold or immunofluorescence labeling options for autophagosomes will be important. Due to the potential ambiguity associated with identifying the cellular degradation machinery, we recommend using at least one additional complementary technique to verify lysosome and autophagosome identity when measuring TEM images. Future studies may also perform quantifications of 3D reconstruction to determine more detailed changes beyond those only shown by TEM.

Using the method outlined here, we have quantified the changes associated with macro autophagy upon treatment with thapsigargin, loss of DRP-1, or knockdown of MARF. Thapsigargin treatment, this is known to cause ER stress and past research has shown that such ER stress promotes lipotoxicity and the formation of lipid droplets [75,76]. Given these previous findings, we believed that autophagy may increase upon thapsigargin treatment in addition to lipid droplets, as previously established for lipid droplets. Specifically, this hypothesized this would come across given that past literature has found that macro autophagy can serve as a protective mechanism for ER stress [77,78]. Our results support the autophagic response to ER stress, as autolysosome, autophagosome, and lysosomes all increased in quantity in three different models (Figure 3). Critically, we also examined size of these organelles, as past literature has also suggested that the size of these organelles relates to their efficiency and function [37,79,80]. In combination, our results show in all three models a large increase in autophagy machinery. ER stress is typically caused by dysregulation of protein folding, causing dysregulation of ER homeostasis [77]. In response, the unfolded protein response is activated, which can have a downstream effect of increasing autophagy to remove defective organelle and macromolecules [81]. Similarly, loss of DRP-1 also was demonstrated to cause an increase in autophagy as seen by increases in size and quantity of organelles and increased LAMP1 expression (Figure 4), and autophagy likely increases through a similar mechanism. Increased LDs have previously been described as a downstream effect of autophagy, consistent with the conclusion that autophagy occurs more frequently following DRP-1 ablation [32]. Increased autophagy may be due to dysfunctional regulation of mitochondrial length, which is seen in response to loss of DRP-1 regulated fission [32,62]. These results suggest that DRP-1 ablation and the resulting lack of mitochondrial fission increase autophagy in cells, demonstrated by upregulation of the cellular degradation machinery. In past studies, mice lacking DRP-1 have had increased accumulation of damaged mitochondria [63], which may induce increased mitophagy and relevant recycling

machinery. While DRP-1 is typically associated for regulation of mitochondrial fission [43], past literature has also implicated the loss of DRP-1 with ER stress [82]. Specifically, this may come as a result of loss of calcium homeostasis between the dysfunctional mitochondria and ER. Therefore, this is a possible reason for why loss of DRP-1 mimics the changes seen upon thapsigargin treatment. Similarly, past research has also shown that MFN-2 increases ER stress [83]. found that loss of MARF, the fly homolog of MFN2, increased autophagic organelles, further showing a potential increase in autophagy due to ER stress due to the unfolded protein response. Future research may consider studying specificically ER-phagy with this method to better understand how ER-stress activates autophagy, and verify that DRP-1 and MARF loss increase autophagy as a downstream effect of ER stress.

Although limitations of this TEM analysis and SBF-SEM visualization method exist, when combined with other techniques, reliable identification and quantitation of cellular degradation machinery components may be possible. On a broader scale, this method using ImageJ and/or Amira may be applied to other fields with a focus on organelle structure. For example, mitochondria play key roles in many complex diseases, including type II diabetes, cardiomyopathy, and Alzheimer's disease [35,36,53–56] and autophagy may contribute to these diseases, given its role in mitophagy to clear dysfunctional mitochondria. Use of TEM and ImageJ to study other organelles in conjunction with the precise methodology outlined here to study key autophagic organelles will improve our understanding of the physiology associated with key organelles and their contributions to disease.

6 Perspective on Staining

Lysosome stages may look different when using different EM staining procedures, depending on the material used for preparation (e.g., osmium tetroxide) and the type and amount of additives used (e.g., uranyl acetate, lead citrate, and ruthenium red). Depending on the stain used, lysosomal membrane contrast may be altered, affecting the appearance of lysosome-related structures. All EM images shown here used a grid-based staining technique in all procedures (Table 2). The general TEM sample preparation protocol used glutaraldehyde and 1% osmium tetroxide as fixatives [84–87]. Post staining on TEM ultrathin sections used 5% uranyl acetate for 6 min to increase membrane contrast and Reynold's Lead Citrate for 3 min to improve resolution of cellular structures [88–90]. Other stains may be used to optimize the experimental purpose, and staining time should be adjusted according to the sample type. Other viable alternatives exist; for example, ruthenium tetroxide is particularly useful when preparing kidney, liver, and prostate tissue [91,92]. Ammoniated ruthenium oxychloride, commonly referred to as ruthenium red, is frequently used as a polycationic dye to stain negatively charged molecules, including polysaccharides, in tissue sections [93–95]. Although ruthenium red is commonly used for fungal staining, when used with osmium tetroxide, a chemical reaction occurs that may increase the contrast of TEM micrographs [93–95]. Regardless of the stain used, the foremost concern should be maintaining consistency in tissue staining. Different staining in the same organism for example, staining separately for lysosomes, should be avoided. Ideally, the same staining solution should be used for all samples, even at different stages, making it possible to compare different times or stages. If staining protocols different from those described here are used, lysosome appearance may vary.

7 Conflict of Interest

The authors declare that the research was conducted in the absence of any commercial or financial relationships that could be construed as a potential conflict of interest.

8 Author Contributions

Conceptualization, E.G.-L., Z.V., P.K., J.S. (Jianqiang Shao), R.O.P., E.D.A. and A.H.J.;
Methodology, E.G.-L., Z.V., P.K., L.V., J.S. (Jianqiang Shao), S.A., M.M., M.B., S.A.M., J.L., T.A.C., J.L.S., R.O.P., E.D.A. and A.H.J.; software, E.G.-L., Z.V., P.K., L.V., T.A.C., J.L.S., R.O.P., E.D.A. and A.H.J.;
Validation, E.G.-L., Z.V., P.K., K.N., L.V., T.A.C., J.L.S., J.S. (Jianqiang Shao), R.O.P., E.D.A. and A.H.J.;
Formal analysis, E.G.-L., Z.V., P.K., K.N., L.V., J.S. (Jianqiang Shao), T.A.C., J.L.S., R.O.P., E.D.A. and A.H.J.;
Investigation, E.G.-L., Z.V., P.K., L.V., J.S. (Jianqiang Shao), H.K.B., A.G.M., T.A.R., T.A.C., J.L.S., B.G., J.S. (Jennifer Streeter), R.O.P., E.D.A. and A.H.J.;
Resources, E.G.-L., Z.V., P.K., S.A.M., T.A.C., J.L.S., R.O.P., E.D.A. and A.H.J.;
Data curation, E.G.-L., Z.V., P.K., J.S. (Jennifer Streeter), H.K.B., A.G.M., T.A.R., R.O.P., E.D.A. and A.H.J.;
Writing—original draft preparation, E.G.-L., Z.V., P.K., K.N., H.K.B., A.G.M., T.A.R., M.B., S.A.M., B.G., T.A.C., J.L.S., R.O.P., E.D.A. and A.H.J.;
Writing—review and editing, E.G.-L., Z.V., P.K., K.N., H.K.B., A.G.M., T.A.R., S.A.M., B.G., T.A.C., J.L.S., R.O.P., E.D.A. and A.H.J.;
Visualization, E.G.-L., Z.V., P.K., K.N., B.G., T.A.C., J.L.S., R.O.P., E.D.A. and A.H.J.;
Supervision, E.G.-L., Z.V., P.K., B.G., T.A.C., J.L.S., R.O.P., E.D.A. and A.H.J.;
Project administration, E.G.-L., Z.V., P.K., T.A.C., J.L.S., R.O.P., E.D.A. and A.H.J.;
Funding acquisition, E.D.A. and A.H.J.
All authors have read and agreed to the published version of the manuscript.

9 Funding

This work was supported by NIH grants, R01HL108379 and R01DK092065 to E.D.A. UNCF/BMS EE United Negro College Fund/Bristol–Myers Squibb EE Just Postgraduate Fellowship in the Life Sciences Fellowship to H.K.B., the United Negro College Fund/Bristol–Myers Squibb EE Just Faculty Fund, Burroughs Wellcome Fund Career Awards at the Scientific Interface Award, Burroughs Wellcome Fund Ad-hoc Award, the National Institutes of Health Small Research Pilot Subaward 5R25HL106365-12 from the National Institutes of Health PRIDE Program, DK020593, the Vanderbilt Diabetes and Research Training Center for DRTC Alzheimer's Disease Pilot & Feasibility Program to A.H.J. The NSF grant MCB 2011577I and NIH T32 5T32GM133353 to S.A.M.Acknowledgments

We would also like to thank our undergraduate colleagues Benjamin Kirk and Innes Hicsasmaz for helping to optimize the analysis technique. y

References

1 Ryter, S.W. *et al.* (2019) Autophagy: a lysosome-dependent process with implications in cellular redox homeostasis and human disease. *Antioxidants & redox signaling* 30, 138–159

2 Yin, Z. *et al.* (2016) Autophagy: machinery and regulation. *Microbial cell* 3, 588

3 Levy, J.M.M. and Thorburn, A. (2020) Autophagy in cancer: moving from understanding mechanism to improving therapy responses in patients. *Cell Death & Differentiation* 27, 843–857

4 Eskelinen, E.-L. (2005) Maturation of autophagic vacuoles in mammalian cells. *Autophagy* 1, 1–10

5 Bernard, A. and Klionsky, D.J. (2013) Autophagosome formation: tracing the source. *Developmental cell* 25, 116–117

6 Ganesan, D. and Cai, Q. (2021) Understanding amphisomes. *Biochemical Journal* 478, 1959–1976

7 (2013) Amphisomes: out of the autophagosome shadow? *The EMBO Journal* 32, 3116–3118

8 Yu, L. *et al.* (2010) Termination of autophagy and reformation of lysosomes regulated by mTOR. *Nature* 465, 942–946

9 Yu, L. *et al.* (2018) Autophagy pathway: cellular and molecular mechanisms. *Autophagy* 14, 207–215

10 Jung, M. *et al.* (2019) The autophagy research in electron microscopy. *Applied Microscopy* 49, 1–7

11 Lam, J. *et al.* (2021) A Universal Approach to Analyzing Transmission Electron Microscopy with ImageJ. *bioRxiv*

12 Eskelinen, E.-L. *et al.* (2011) Seeing is believing: the impact of electron microscopy on autophagy research. *Autophagy* 7, 935–956

13 Rasband, W.S. (2011) Imagej, us national institutes of health, bethesda, maryland, usa. *http://imagej. nih. gov/ij/*

14 Cocks, E. *et al.* (2018) A guide to analysis and reconstruction of serial block face scanning electron microscopy data. *Journal of microscopy* 270, 217–234

15 Hughes, L. *et al.* (2014) Serial block face scanning electron microscopy—the future of cell ultrastructure imaging. *Protoplasma* 251, 395–401

16 Garza-Lopez, E. *et al.* (2022) Protocols for Generating Surfaces and Measuring 3D Organelle Morphology Using Amira. *Cells* 11, 65

17 Trivedi, P.C. *et al.* (2020) Lysosomal biology and function: modern view of cellular debris bin. *Cells* 9, 1131

18 Klionsky, D.J. and Eskelinen, E.-L. (2014) The vacuole vs. the lysosome: When size matters. *Autophagy* 10, 185–187

19 Bandyopadhyay, D. *et al.* (2014) Lysosome transport as a function of lysosome diameter. *PloS one* 9, e86847

20 Matteoni, R. and Kreis, T.E. (1987) Translocation and clustering of endosomes and lysosomes depends on microtubules. *Journal of Cell Biology* 105, 1253–1265

21 Heuser, J. (1989) Changes in lysosome shape and distribution correlated with changes in cytoplasmic pH. *Journal of Cell Biology* 108, 855–864

22 Cuervo, A.M. and Dice, J.F. (2000) When lysosomes get old☆. *Experimental gerontology* 35, 119–131

23 Talsma, H. *et al.* (1987) Multilamellar or multivesicular vesicles? *International journal of pharmaceutics* 37, 171–173

24 Cui, Y. *et al.* (2018) The multivesicular body and autophagosome pathways in plants. *Frontiers in plant science* 9, 1837

25 Fader, C. and Colombo, M. (2009) Autophagy and multivesicular bodies: two closely related partners. *Cell Death & Differentiation* 16, 70–78

26 Eskelinen, E.-L. (2008) To be or not to be? Examples of incorrect identification of autophagic compartments in conventional transmission electron microscopy of mammalian cells. *Autophagy* 4, 257–260

27 Ray, K. (2010) "Empty" autophagosomes fail to carry their cargo in Huntington disease. *Nat Rev Neurol* 6, 298–298

28 Clokey, G.V. and Jacobson, L.A. (1986) The autofluorescent "lipofuscin granules" in the intestinal cells of Caenorhabditis elegans are secondary lysosomes. *Mechanisms of ageing and development* 35, 79–94

29 Wang, H. *et al.* (2016) TFEB overexpression in the P301S model of tauopathy mitigates increased PHF1 levels and lipofuscin puncta and rescues memory deficits. *eneuro* 3,

30 Suzuki, K. *et al.* (2014) Proteomic profiling of autophagosome cargo in Saccharomyces cerevisiae. *PLoS One* 9, e91651

31 Gatica, D. *et al.* (2018) Cargo recognition and degradation by selective autophagy. *Nature cell biology* 20, 233–242

32 Nguyen, T.B. and Olzmann, J.A. (2017) Lipid droplets and lipotoxicity during autophagy. *Autophagy* 13, 2002–2003

33 Olzmann, J.A. and Carvalho, P. (2019) Dynamics and functions of lipid droplets. *Nature reviews Molecular cell biology* 20, 137–155

34 Qi, Z. and Chen, L. (2019) Endoplasmic reticulum stress and autophagy. *Autophagy: Biology and Diseases*

35 Eura, Y. *et al.* (2003) Two mitofusin proteins, mammalian homologues of FZO, with distinct functions are both required for mitochondrial fusion. *Journal of biochemistry* 134, 333–344

36 Hales, K.G. and Fuller, M.T. (1997) Developmentally regulated mitochondrial fusion mediated by a conserved, novel, predicted GTPase. *Cell* 90, 121–129

37 Kim, S. *et al.* (2020) Quantitative and qualitative analysis of autophagy flux using imaging. *BMB reports* 53, 241

38 Arai, R. and Waguri, S. (2019) Improved electron microscopy fixation methods for tracking autophagy-associated membranes in cultured mammalian cells. In *Autophagy* pp. 211–221, Springer

39 Hamasaki, M. *et al.* (2013) Autophagosomes form at ER–mitochondria contact sites. *Nature* 495, 389–393

40 Ylä-Anttila, P. *et al.* (2009) Monitoring autophagy by electron microscopy in Mammalian cells. *Methods in enzymology* 452, 143–164

41 Pereira, R.O. *et al.* (2017) OPA 1 deficiency promotes secretion of FGF 21 from muscle that prevents obesity and insulin resistance. *The EMBO journal* 36, 2126–2145

42 Southard, S. *et al.* (2014) A series of Cre-ERT2 drivers for manipulation of the skeletal muscle lineage. *genesis* 52, 759–770

43 Favaro, G. *et al.* (2019) DRP1-mediated mitochondrial shape controls calcium homeostasis and muscle mass. *Nature communications* 10, 1–17

44 Katti, P. *et al.* (2021) Marf-mediated mitochondrial fusion is imperative for the development and functioning of indirect flight muscles (IFMs) in drosophila. *Experimental Cell Research* 399, 112486

45 Han, J. *et al.* (2013) ER-stress-induced transcriptional regulation increases protein synthesis leading to cell death. *Nature cell biology* 15, 481–490

46 Galmes, R. *et al.* (2016) ORP5/ORP8 localize to endoplasmic reticulum–mitochondria contacts and are involved in mitochondrial function. *EMBO reports* 17, 800–810

47 Chazotte, B. (2011) Labeling lysosomes in live cells with LysoTracker. *Cold Spring Harbor Protocols* 2011, pdb-prot5571

48 Delrue, R. *et al.* (2001) Identification of Brucella spp. genes involved in intracellular trafficking. *Cellular microbiology* 3, 487–497

49 McDowell, E. and Trump, B. (1976) Histologic fixatives suitable for diagnostic light and electron microscopy. *Archives of pathology & laboratory medicine* 100, 405–414

50 Parra, V. *et al.* (2014) Insulin stimulates mitochondrial fusion and function in cardiomyocytes via the Akt-mTOR-NFκB-Opa-1 signaling pathway. *Diabetes* 63, 75–88

51 Pasqua, T. *et al.* (2016) Impact of Chromogranin A deficiency on catecholamine storage, catecholamine granule morphology and chromaffin cell energy metabolism in vivo. *Cell and tissue research* 363, 693–712

52 Vincent, A.E. *et al.* (2019) Quantitative 3D mapping of the human skeletal muscle mitochondrial network. *Cell reports* 26, 996–1009

53 Mozdy, A.D. and Shaw, J.M. (2003) A fuzzy mitochondrial fusion apparatus comes into focus. *Nature reviews Molecular cell biology* 4, 468–478

54 Rojo, M. *et al.* (2002) Membrane topology and mitochondrial targeting of mitofusins, ubiquitous mammalian homologs of the transmembrane GTPase Fzo. *Journal of cell science* 115, 1663–1674

55 Santel, A. and Fuller, M.T. (2001) Control of mitochondrial morphology by a human mitofusin. *Journal of cell science* 114, 867–874

56 Santel, A. *et al.* (2003) Mitofusin-1 protein is a generally expressed mediator of mitochondrial fusion in mammalian cells. *Journal of cell science* 116, 2763–2774

57 Klionsky, D.J. *et al.* (2008) Guidelines for the use and interpretation of assays for monitoring autophagy in higher eukaryotes. *Autophagy* 4, 151–175

58 Kabeya, Y. *et al.* (2000) LC3, a mammalian homologue of yeast Apg8p, is localized in autophagosome membranes after processing. *The EMBO journal* 19, 5720–5728

59 Jager, S. *et al.* (2004) Role for Rab7 in maturation of late autophagic vacuoles. *Journal of cell science* 117, 4837–4848

60 Botos, E. *et al.* (2008) Caveolin-1 is transported to multi-vesicular bodies after albumin-induced endocytosis of caveolae in HepG2 cells. *Journal of cellular and molecular medicine* 12, 1632–1639

911 61 Lindner, P. *et al.* (2020) Cell death induced by the ER stressor thapsigargin involves death
912 receptor 5, a non-autophagic function of MAP1LC3B, and distinct contributions from unfolded
913 protein response components. *Cell Communication and Signaling* 18, 1–23

914 62 Ikeda, Y. *et al.* (2015) Endogenous Drp1 mediates mitochondrial autophagy and protects the
915 heart against energy stress. *Circulation research* 116, 264–278

916 63 Zuo, W. *et al.* (2014) Mitochondria autophagy is induced after hypoxic/ischemic stress in a Drp1
917 dependent manner: the role of inhibition of Drp1 in ischemic brain damage. *Neuropharmacology*
918 86, 103–115

919 64 Cheng, X.-T. *et al.* (2018) Revisiting LAMP1 as a marker for degradative autophagy-lysosomal
920 organelles in the nervous system. *Autophagy* 14, 1472–1474

921 65 Casellas-Díaz, S. *et al.* (2021) Mfn2 localization in the ER is necessary for its bioenergetic
922 function and neuritic development. *EMBO reports*

923 66 Muñoz, J.P. *et al.* (2013) Mfn2 modulates the UPR and mitochondrial function via repression of
924 PERK. *The EMBO journal* 32, 2348–2361

925 67 Shen, J.L. *et al.* (2021) Vmp1, Vps13D, and Marf/Mfn2 function in a conserved pathway to
926 regulate mitochondria and ER contact in development and disease. *Current Biology*

927 68 Zhao, T. *et al.* (2012) Central role of mitofusin 2 in autophagosome-lysosome fusion in
928 cardiomyocytes. *Journal of Biological Chemistry* 287, 23615–23625

929 69 Sugiura, A. *et al.* (2014) A new pathway for mitochondrial quality control: mitochondrial-derived
930 vesicles. *The EMBO journal* 33, 2142–2156

931 70 Martinet, W. *et al.* (2014) Methods to assess autophagy in situ—transmission electron
932 microscopy versus immunohistochemistry. *Methods in enzymology* 543, 89–114

933 71 Allaire, A. *et al.* (2015) Immunofluorescence to monitor the cellular uptake of human lactoferrin
934 and its associated antiviral activity against the hepatitis C virus. *Journal of visualized*
935 *experiments: JoVE*

936 72 Odell, I.D. and Cook, D. (2013) Immunofluorescence techniques. *The Journal of investigative*
937 *dermatology* 133, e4

938 73 Nair, U. *et al.* (2012) A role for Atg8–PE deconjugation in autophagosome biogenesis.
939 *Autophagy* 8, 780–793

940 74 Listenberger, L.L. *et al.* (2016) Fluorescent detection of lipid droplets and associated proteins.
941 *Current Protocols in Cell Biology* 71, 4–31

942 75 Han, J. and Kaufman, R.J. (2016) The role of ER stress in lipid metabolism and lipotoxicity.
943 *Journal of Lipid Research* 57, 1329–1338

944 76 Lee, J.-S. *et al.* (2012) Pharmacological ER stress promotes hepatic lipogenesis and lipid droplet
945 formation. *Am J Transl Res* 4, 102–113

946 77 Rashid, H.-O. *et al.* (2015) ER stress: Autophagy induction, inhibition and selection. *Autophagy*
947 11, 1956–1977

948 78 Song, S. *et al.* (2017) Crosstalk of autophagy and apoptosis: Involvement of the dual role of
949 autophagy under ER stress. *Journal of Cellular Physiology* 232, 2977–2984

950 79 Backues, S.K. *et al.* (2014) Estimating the size and number of autophagic bodies by electron
951 microscopy. *Autophagy* 10, 155–164

80 de Araujo, M.E.G. *et al.* (2020) Lysosomal size matters. *Traffic* 21, 60–75

81 Kabir, M.F. *et al.* (2018) *Endoplasmic Reticulum Stress and Autophagy*, IntechOpen.

82 Wang, L. *et al.* (2021) Dynamin-related protein 1 deficiency accelerates lipopolysaccharide-induced acute liver injury and inflammation in mice. *Commun Biol* 4, 1–14

83 Ngoh, G.A. *et al.* (2012) Loss of mitofusin 2 promotes endoplasmic reticulum stress. *Journal of Biological Chemistry* 287, 20321–20332

84 Franke, W. *et al.* (1969) Simultaneous Glutaraldehyde-Osmium Tetroxide Fixation With Postosmication. An Improved Fixation Procedure for Electron Microscopy of Plant and Animal Cells. *Histochemie. Histochemistry. Histochimie* 19, 162–164

85 Porter, K. and Kallman, F. (1953) The properties and effects of osmium tetroxide as a tissue fixative with special reference to its use for electron microscopy. *Experimental Cell Research* 4, 127–141

86 Cope, G. and Williams, M. (1969) Quantitative studies on the preservation of choline and ethanolamine phosphatides during tissue preparation for electron microscopy: I. Glutaraldehyde, osmium tetroxide, araldite methods. *Journal of microscopy* 90, 31–46

87 White, D. *et al.* (1979) A chemical mechanism for tissue staining by osmium tetroxide-ferrocyanide mixtures. *Journal of Histochemistry & Cytochemistry* 27, 1084–1091

88 Venable, J.H. and Coggeshall, R. (1965) A simplified lead citrate stain for use in electron microscopy. *The Journal of cell biology* 25, 407–408

89 Derksen, J. and Meekes, H. (1984) Selective staining of nucleic acid containing structures by uranyl acetate-lead citrate. *Micron and microscopica acta* 15, 55–58

90 Yamaguchi, M. *et al.* (2005) Repeated use of uranyl acetate solution in section stainingin transmission electron microscopy. *Plant Morphology* 17, 57–59

91 Gaylarde, P. and Sarkany, I. (1968) Ruthenium tetroxide for fixing and staining cytoplasmic membranes. *Science* 161, 1157–1158

92 Headquarters, U.C. Ruthenium Tetroxide.

93 Linss, W. *et al.* (1979) A ruthenium red-osmium tetroxide section staining method (author's transl). *Acta histochemica* 64, 206–212

94 Dierichs, R. (1979) Ruthenium red as a stain for electron microscopy. Some new aspects of its application and mode of action. *Histochemistry* 64, 171–187

95 McKay, A. (1988) A plate assay method for the detection of fungal polygalacturonase secretion. *FEMS Microbiology letters* 56, 355–358

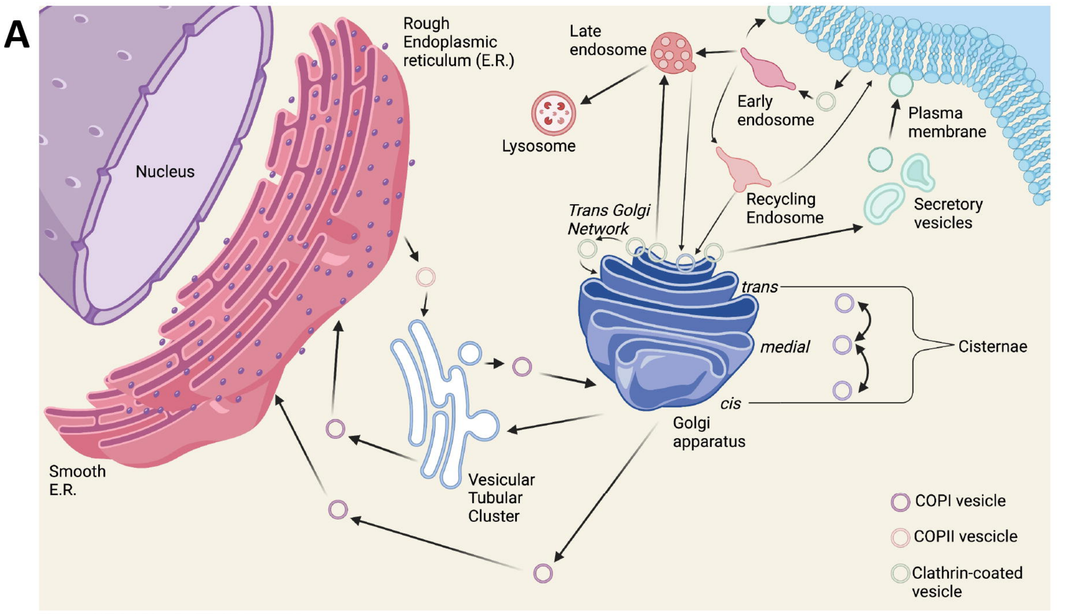

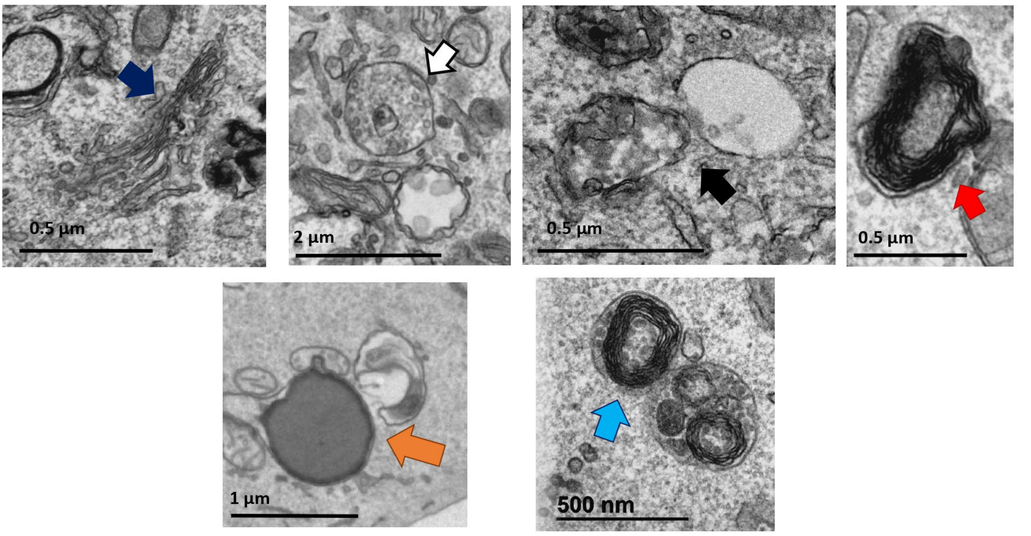

Macroautophagy

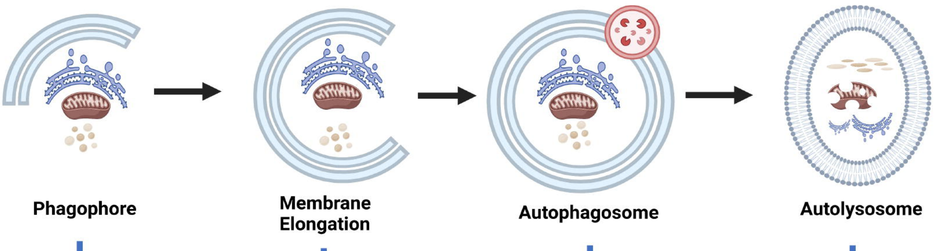

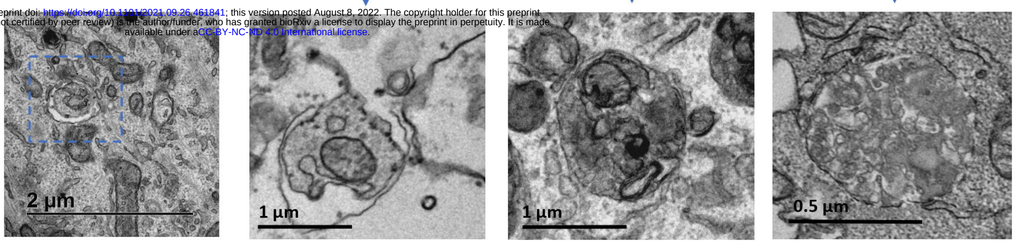

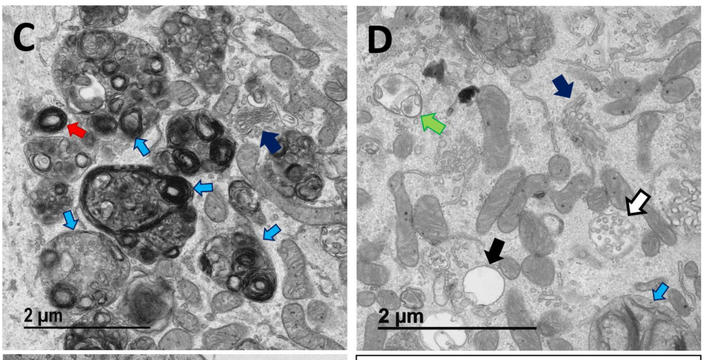

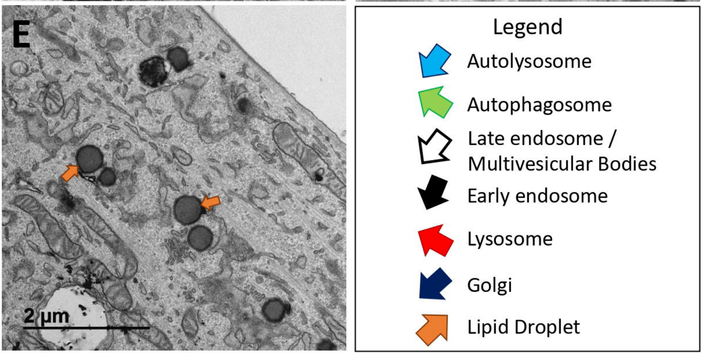

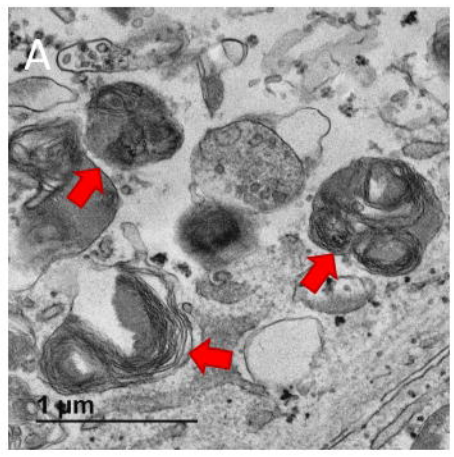

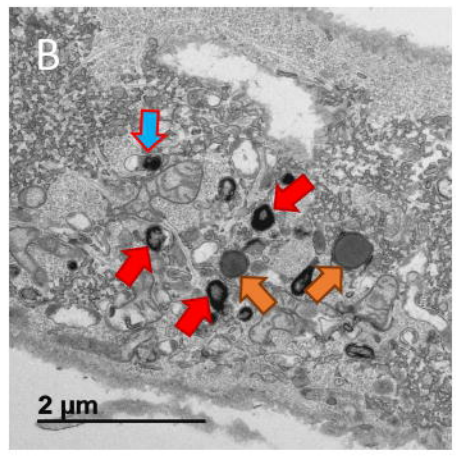

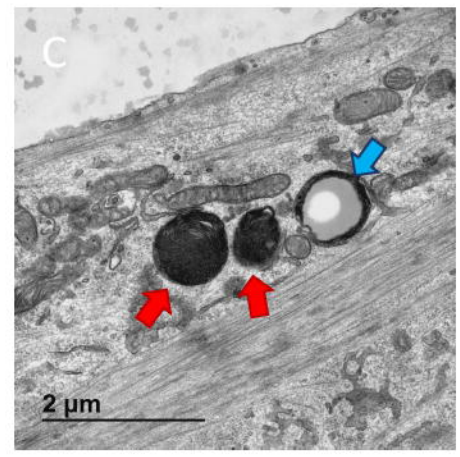

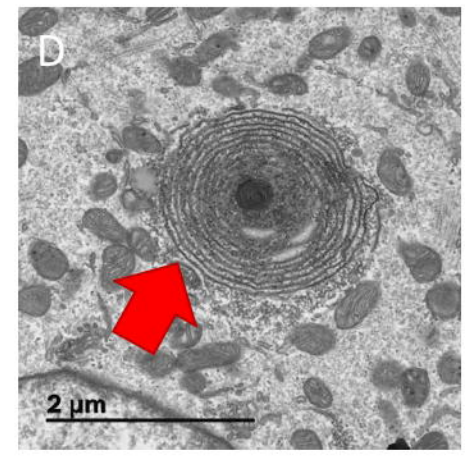

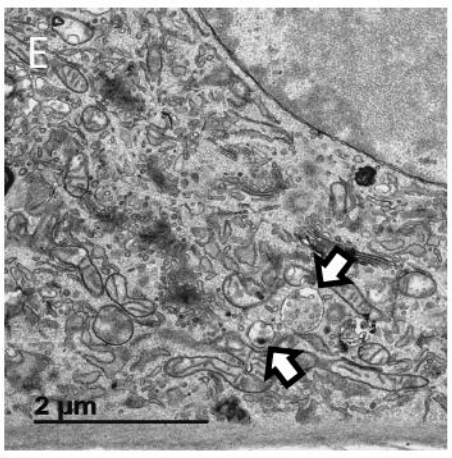

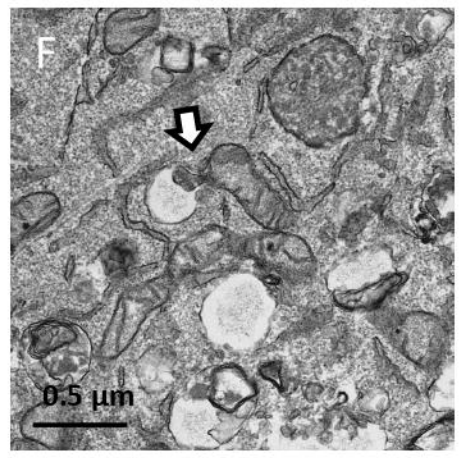

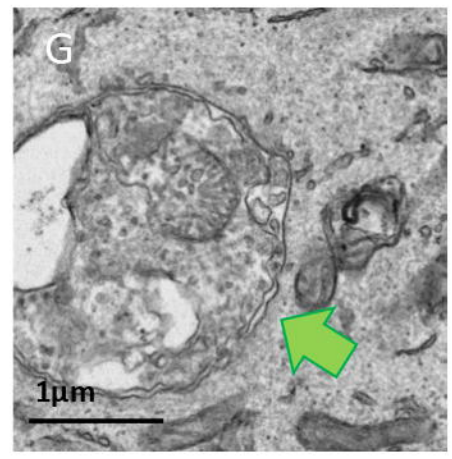

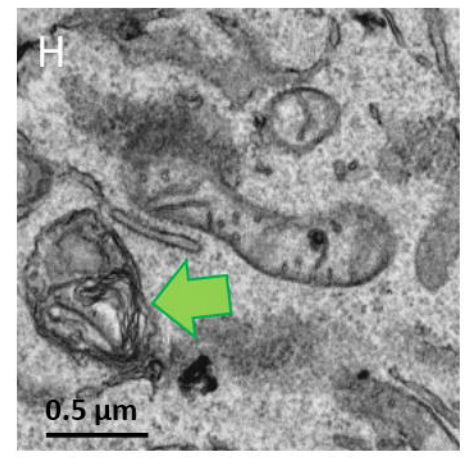

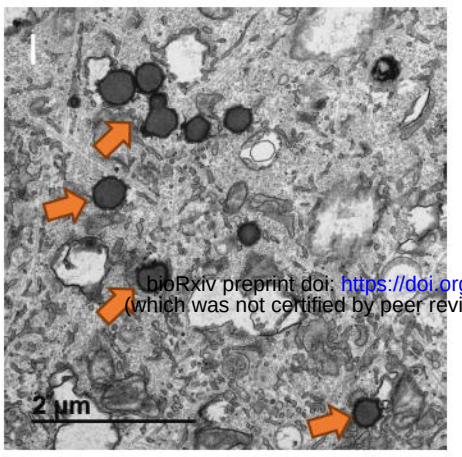

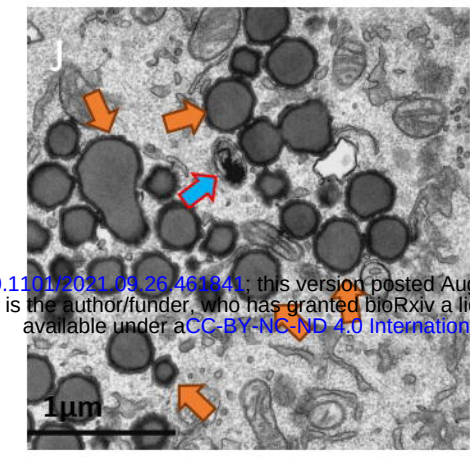

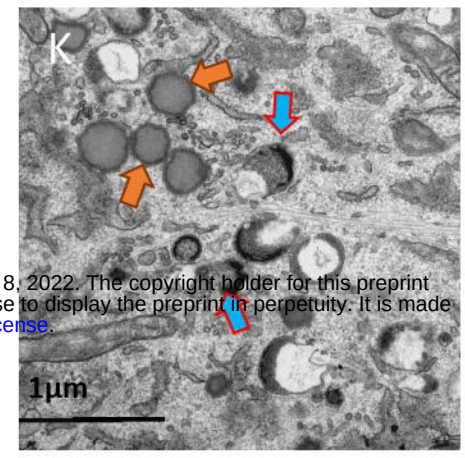

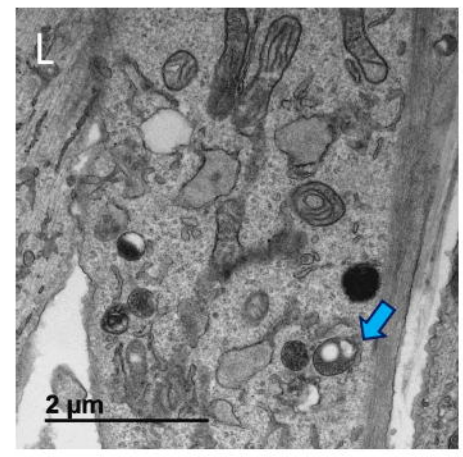

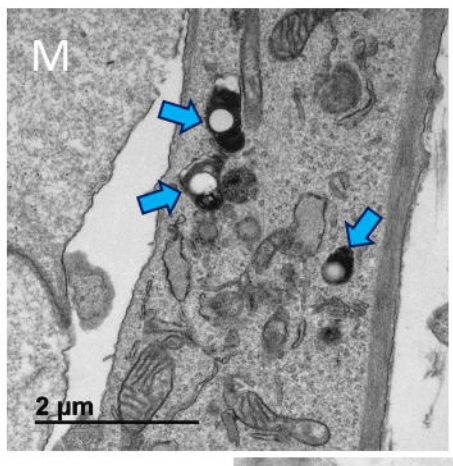

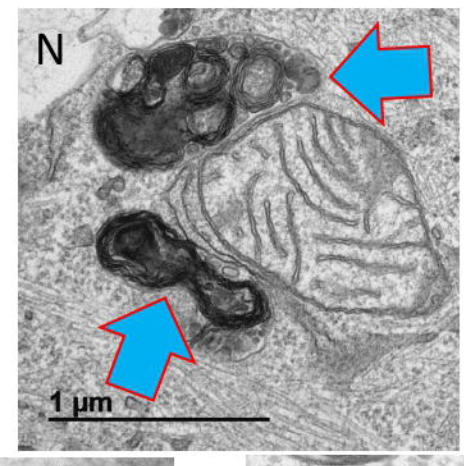

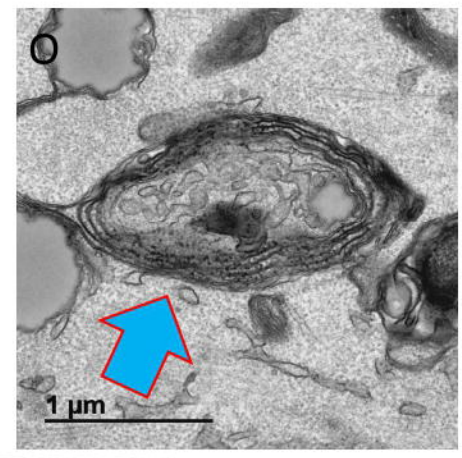

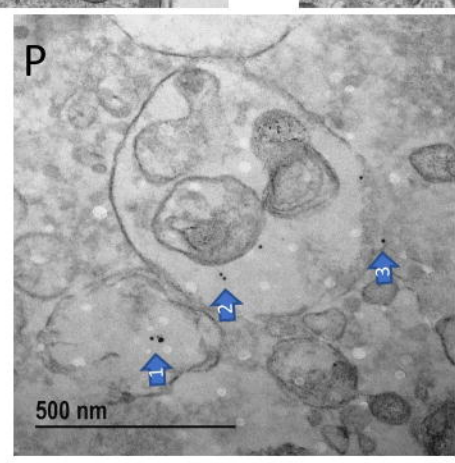

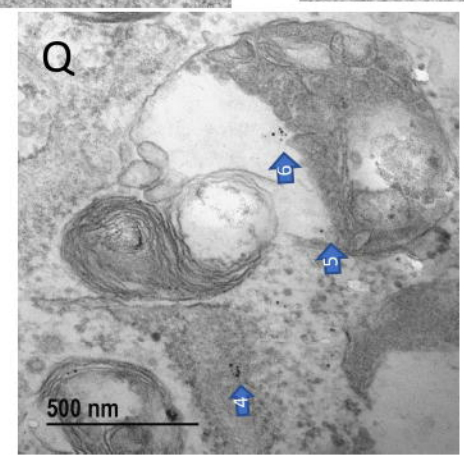

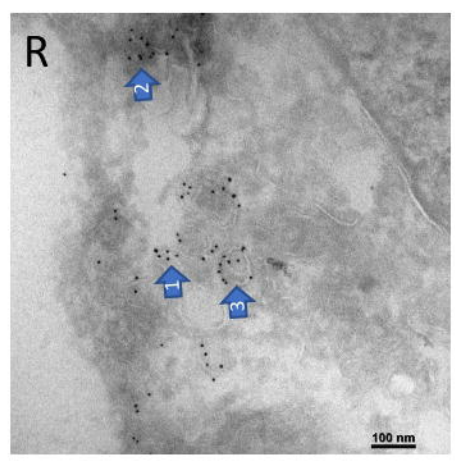

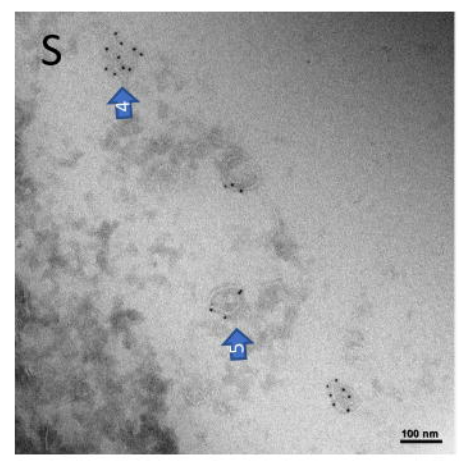

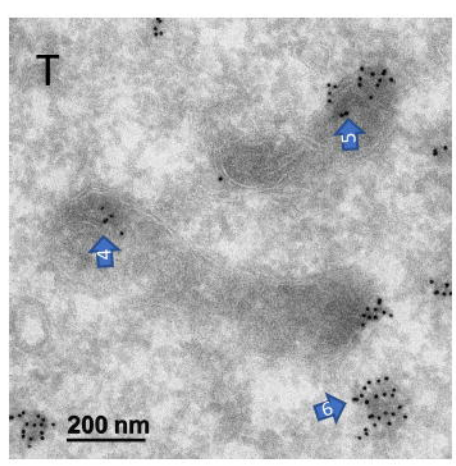

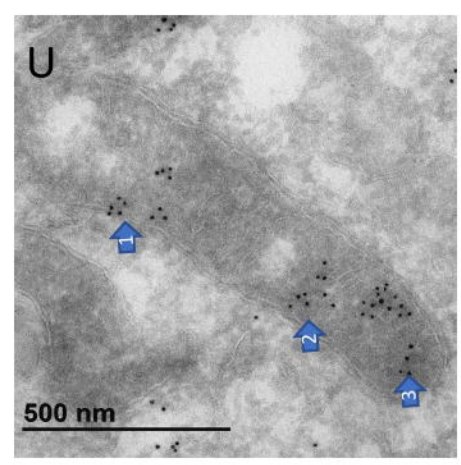

Murine Myotubes

Untreated

+ Thapsgargin

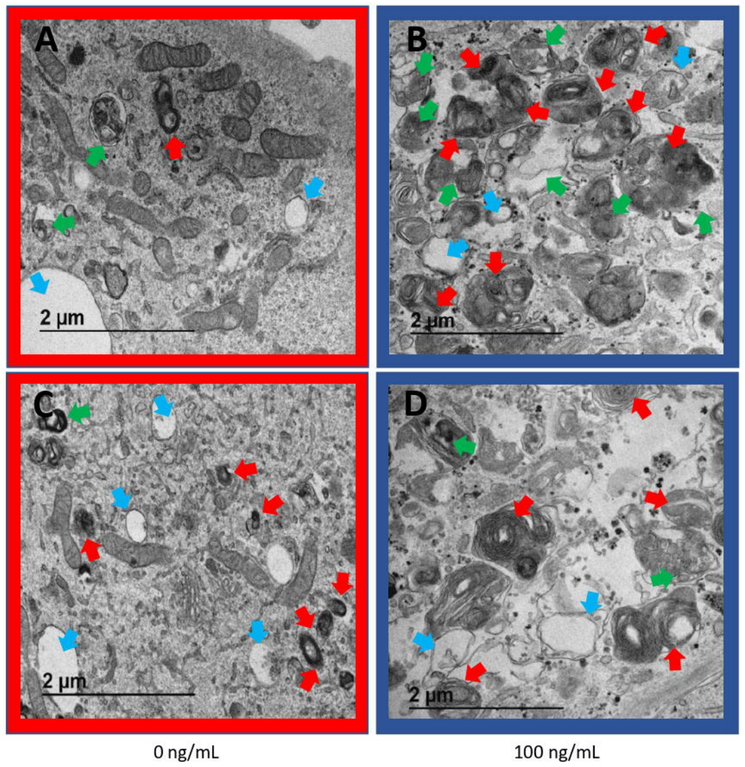

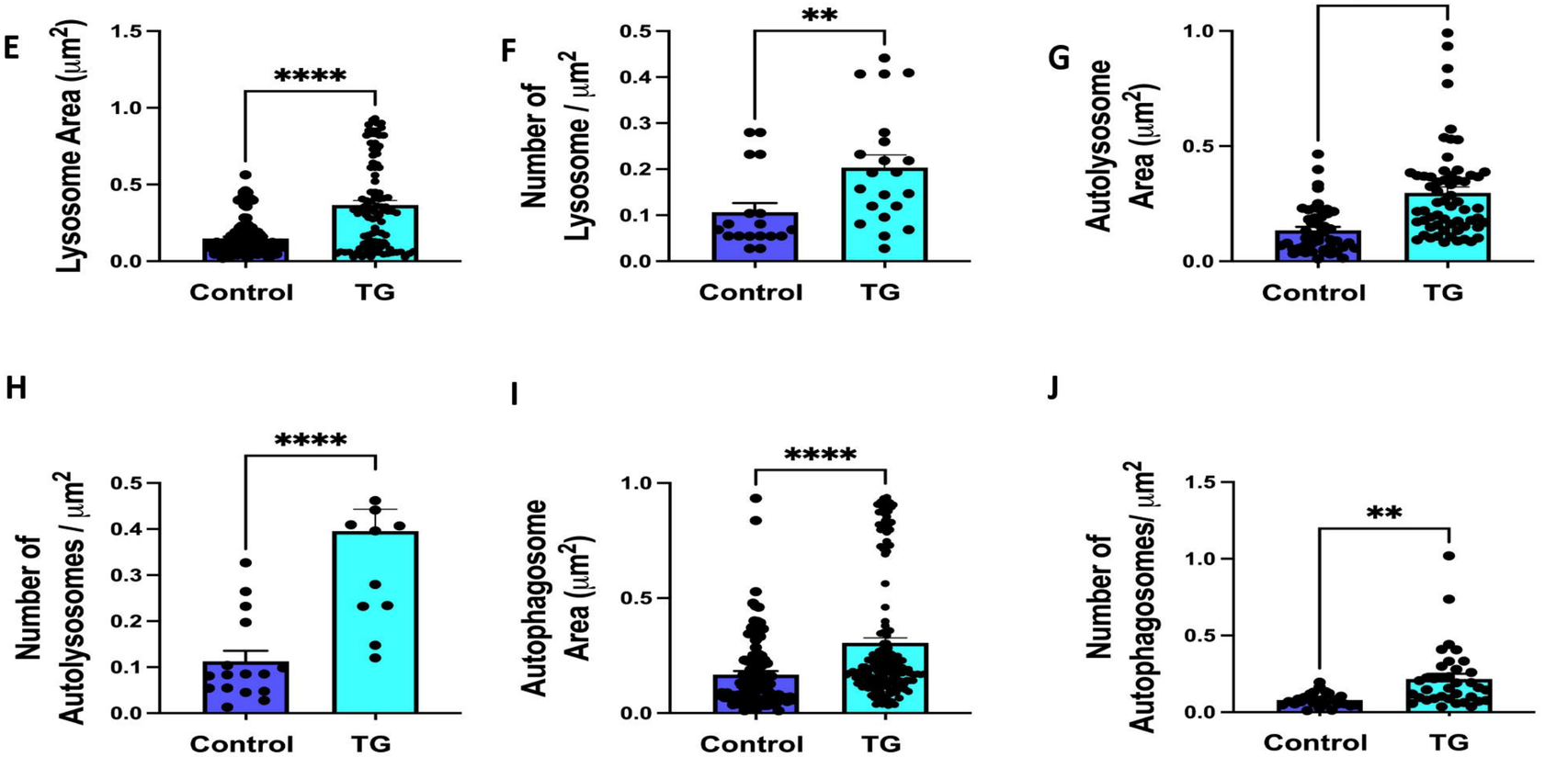

Murine Fibroblasts

Untreated

+ Thapsgargin

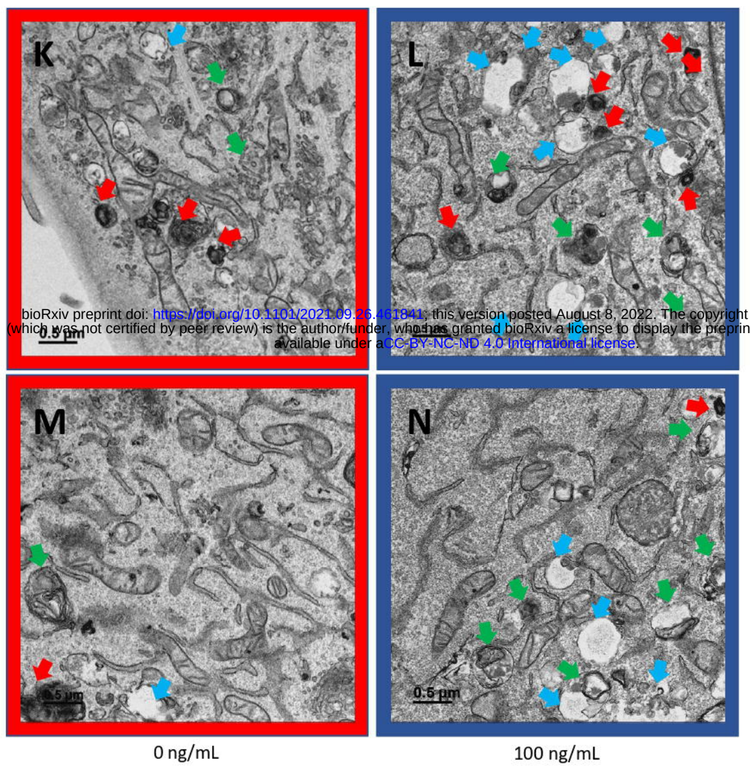

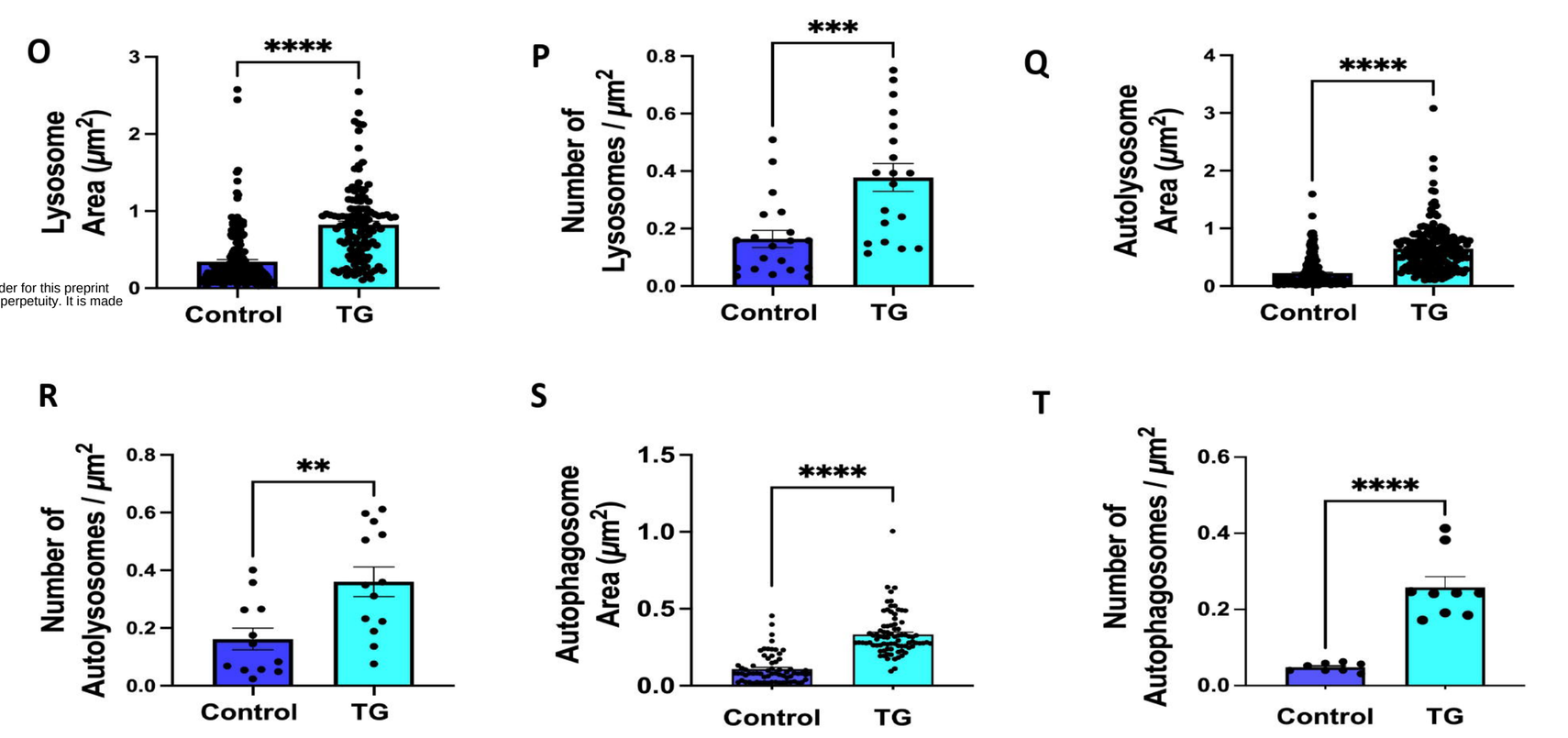

Human Myotubes

Untreated

+ Thapsgargin

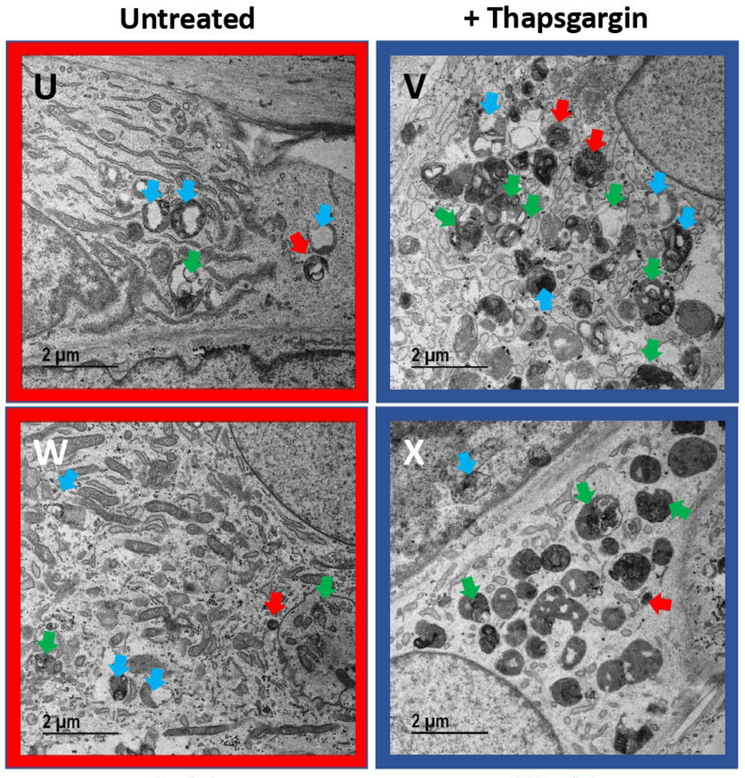

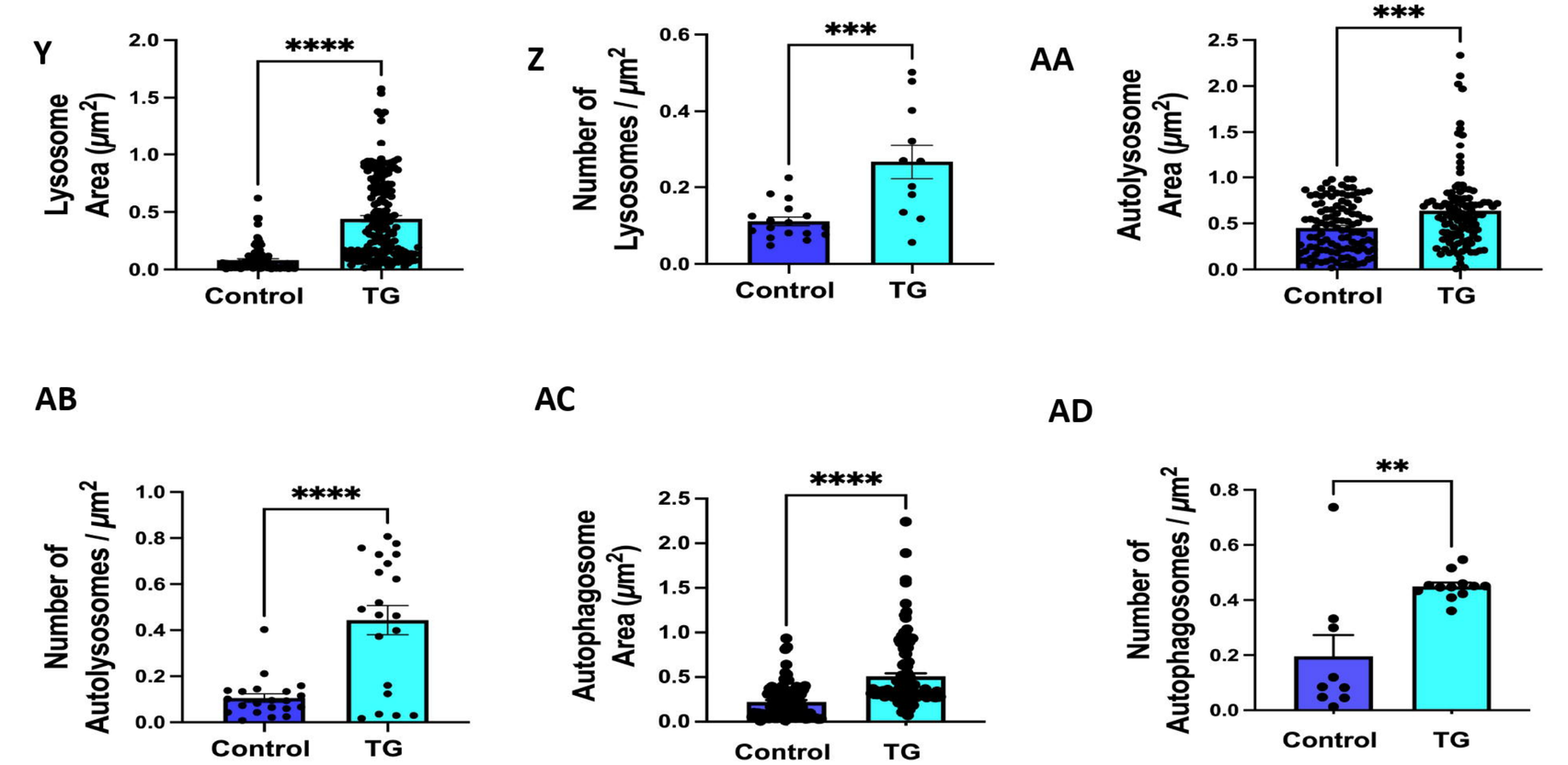

Ad-GFP (WT)

DRP-1smKO (M-cre)

A B C D E F G H I J K L M N O P Q R S T U V W X

Number of Lysosome / μm^2

Lysosome Area (μm^2)

Number of Autophagosomes / μm^2

Autophagosome Area (μm^2)

Number (μm^2)

Area (μm^2)

Volume (μm^3)

Intensity

Sphericity

Length (μm)

WT DRP-1 smKO

Ad-GFP (WT) DRP-1smKO (M-cre) Ad-GFP (WT) DRP-1smKO (M-cre)

Y Z AA AB AC AD AE AF

Y' Z' AA' AB' AC' AD' AE' AF'

Y'' Z'' AA'' AB'' AC'' AD'' AE'' AF''

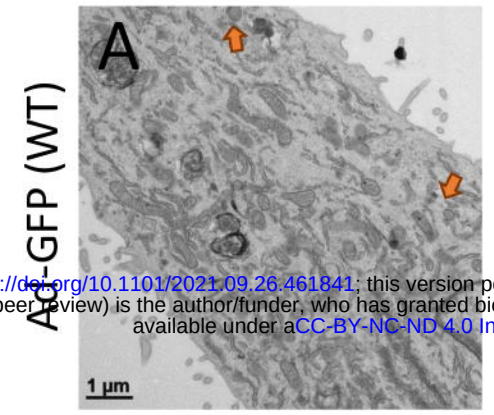

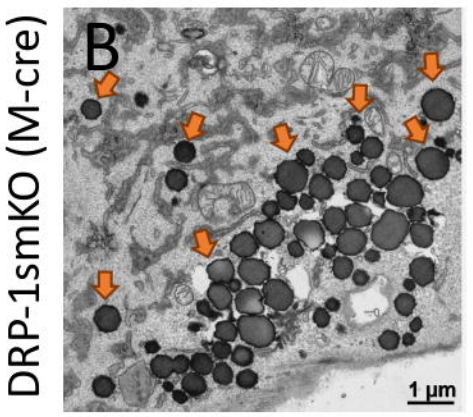

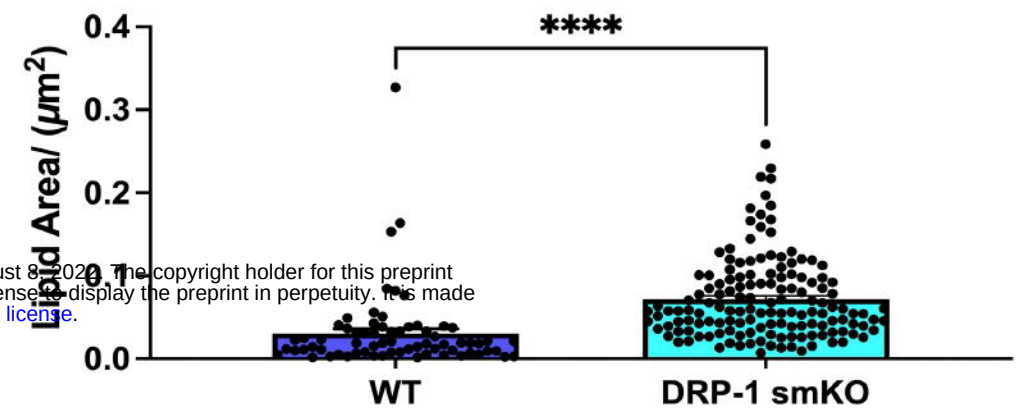

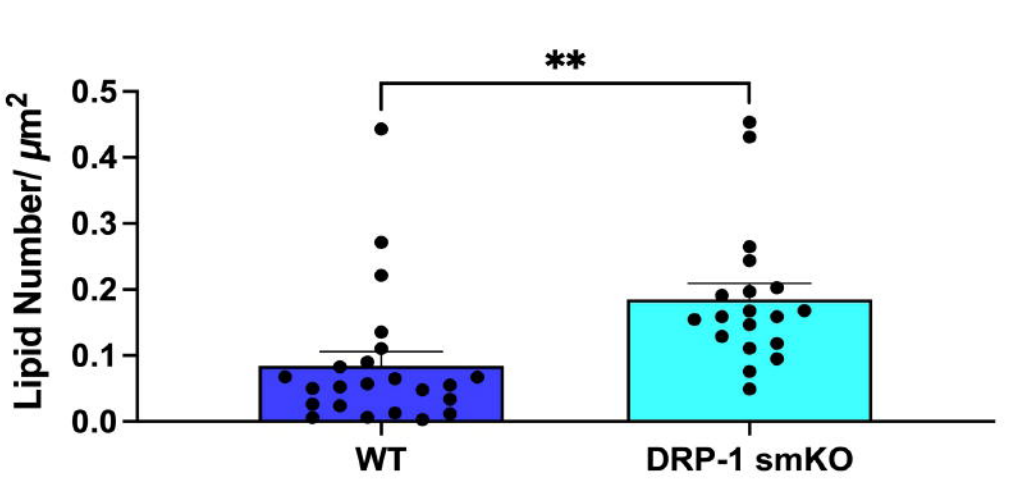

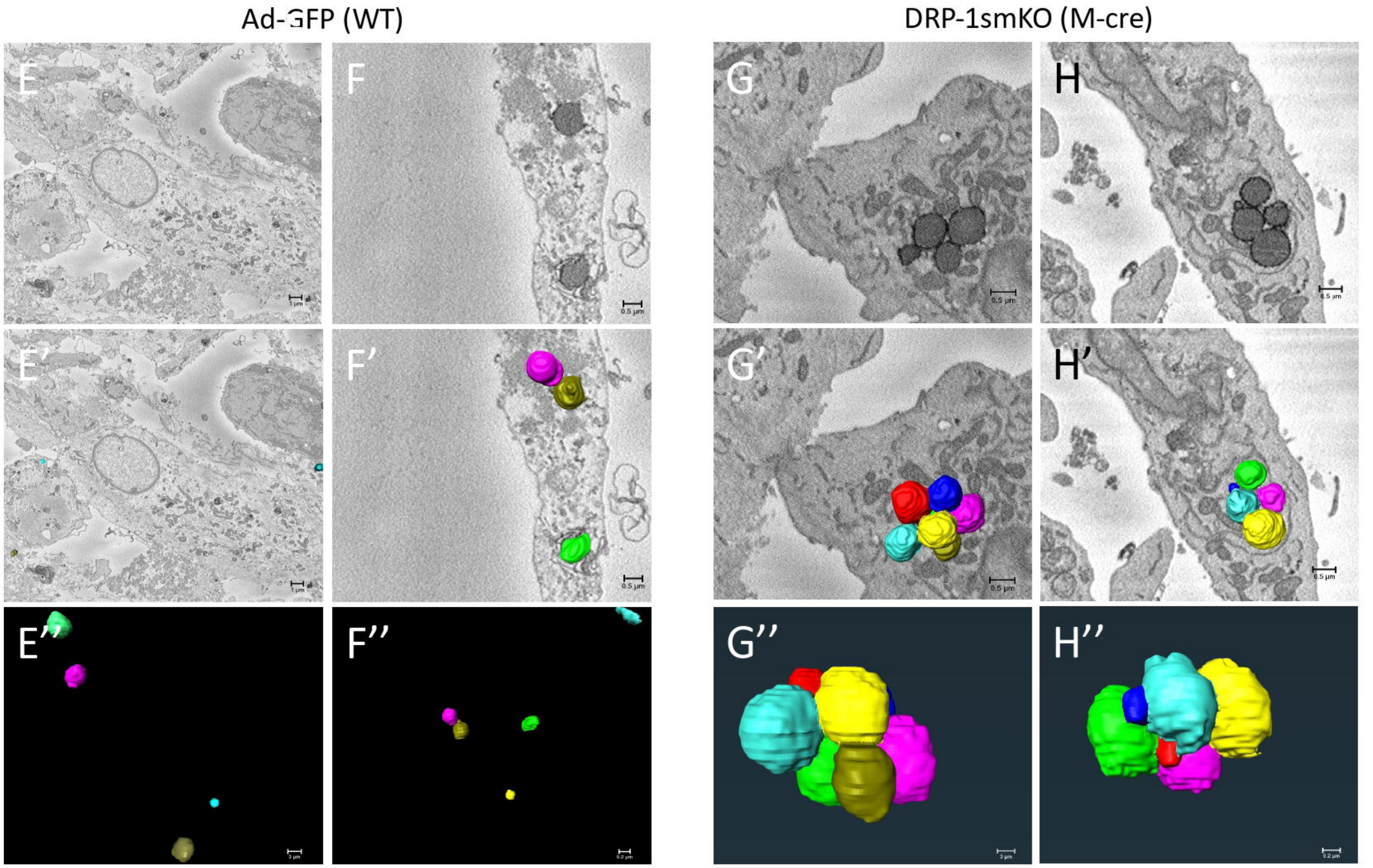

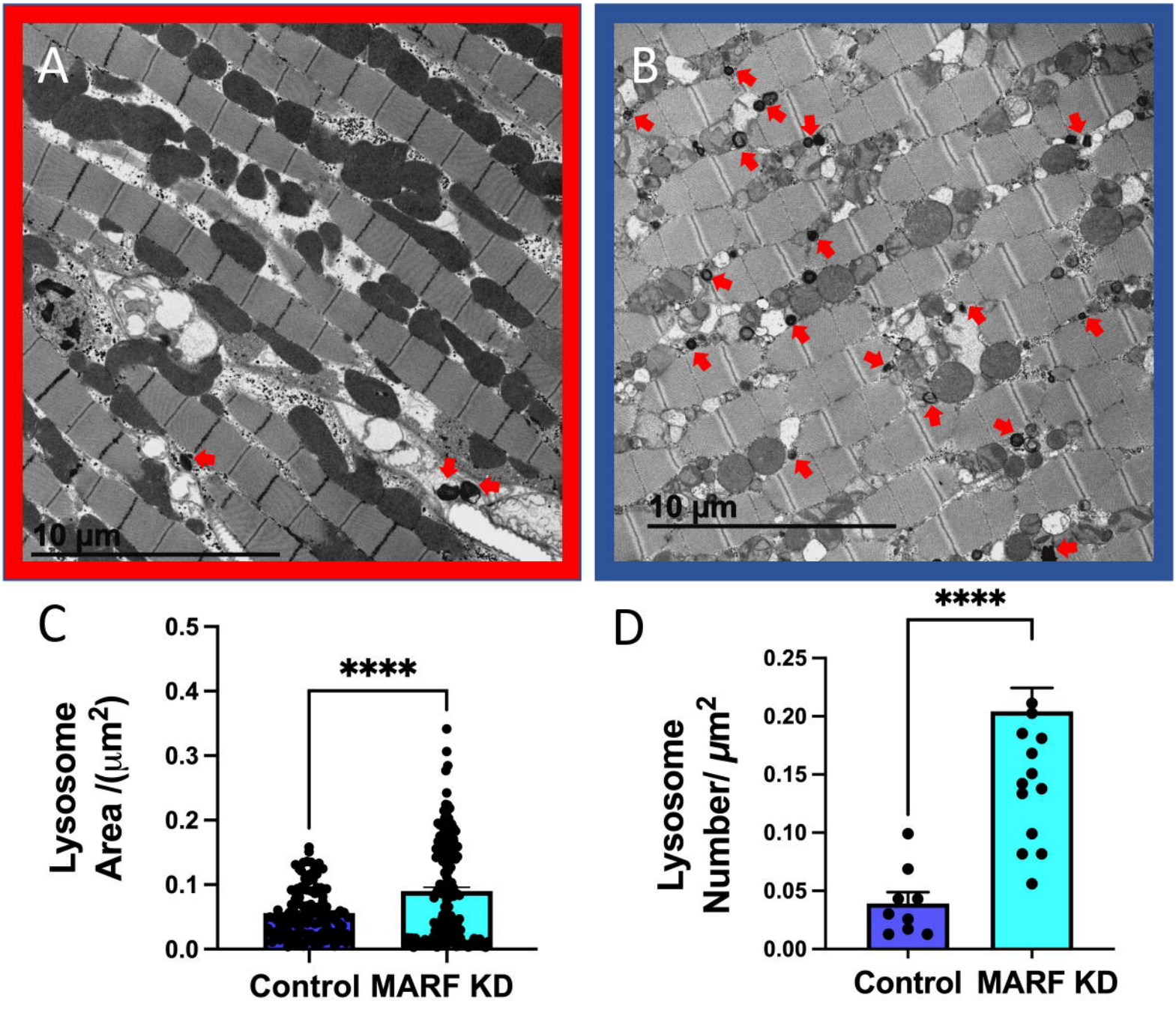
Control
MARF KD
A
10 µm
B
10 µm
C
Lysosome Area /(µm²)
0.5
0.4
0.3
0.2
0.1
0.0
****
Control
MARF KD
D
Lysosome Number/ µm²
0.25
0.20
0.15
0.10
0.05
0.00
****
Control
MARF KD